Pacific Northwest
NATIONAL LABORATORY

PNNL-35856

Assessing Impacts of Waves on Hub-Height Winds off the U.S. West Coast Using Lidar Buoys and Coupled Modeling Approaches

April, 2024

B.J. Gaudet
G. García Medina
R. Krishnamurthy
L. Sheridan
Z. Yang
R. Newsom
M. Pekour
W. Gustafson
J. Liu

U.S. DEPARTMENT OF ENERGY

Prepared for the U.S. Department of Energy
under Contract DE-AC05-76RL01830

DISCLAIMER

PACIFIC NORTHWEST NATIONAL LABORATORY
operated by
BATTELLE
for the
UNITED STATES DEPARTMENT OF ENERGY
under Contract DE-AC05-76RL01830

Printed in the United States of America

Available to DOE and DOE contractors from
the Office of Scientific and Technical Information,
P.O. Box 62, Oak Ridge, TN 37831-0062
www.osti.gov
ph: (865) 576-8401
fox: (865) 576-5728
email: reports@osti.gov

Available to the public from the National Technical Information Service
5301 Shawnee Rd., Alexandria, VA 22312
ph: (800) 553-NTIS (6847)
or (703) 605-6000
email: info@ntis.gov
Online ordering: http://www.ntis.gov

PNNL-35856

Assessing Impacts of Waves on Hub-Height Winds off the U.S. West Coast Using Lidar Buoys and Coupled Modeling Approaches

April, 2024

B.J. Gaudet
G. García Medina
R. Krishnamurthy
L. Sheridan
Z. Yang
R. Newsom
M. Pekour
W. Gustafson
J. Liu

Prepared for
the U.S. Department of Energy
under Contract DE-AC05-76RL01830

Pacific Northwest National Laboratory
Richland, Washington 99354

Abstract

Given the importance of offshore wind energy development to the U.S. clean energy targets, it is vital to be able to characterize the wind resource in that environment accurately. Toward that end, two Bureau of Ocean Energy Management buoys equipped with Doppler lidar are being maintained by Pacific Northwest National Laboratory on behalf of the Department of Energy and deployed to regions of potential offshore wind development. In addition to standard meteorological and oceanographic measurements, the buoys document the wind profile between about 40 m and 250 m above the sea surface through Doppler lidar retrievals. After a multiyear deployment of two buoys along the U.S. East Coast, the buoys were redeployed to the U.S. West coast from 2020 – 2022 to locations near the Humboldt and Morro Bay lease areas. The buoys provide nearly continuous, multiyear datasets that can be used to evaluate predictions of hub-height (~100 m) wind speed for standard atmospheric models in the region.

In the absence of measurements at the study site, offshore wind developers rely on model-based data to assess site conditions. Potential sources of model error in this environment include under-resolution or misrepresentation of coastal topographically forced flows, marine boundary layer dynamics and the evolution of their associated cloud and turbulence fields, the role of upwelling and other currents on surface heat fluxes into the boundary layer, and the impact of wave fields on surface momentum fluxes and thus the wind speed profile. In particular, most predictive models of wind speed do not predict wave fields at all, relying on parameterizations to represent their effects. In thus study, we focus on evaluating the role of wind / wave interactions on modeled hub-height wind speed and error by using the Coupled Ocean–Atmosphere–Wave–Sediment–Transport Modeling System to capture two-way interactions between an atmospheric model (Weather Research and Forecasting (WRF)) and a wave model (WAVEWATCHIII (WW3)) and compare to both stand-alone WRF and one-way coupled WRF / WW3 configurations. Our approach is similar to that used in Gaudet et al. (2022) to evaluate wind / wave coupling over the U.S. East Coast, but applied to the very different environment of the U.S. West Coast.

We show examples for two cases, a cold-season frontal case and a warm-season low-level jet case. We find that wind / wave coupling makes little impact on model error for these cases at the location of the lidar buoys, for which other misrepresentations of model physics seems to be responsible for model-observation discrepancies. However, domain-wide evaluations, which also make use of the National Buoy Data Center network, show that a two-way coupling approach is less prone to systematic errors in the hub-height wind field than the one-way coupled approach. WRF resolution of kilometer-scale or less is needed to properly capture the sharp wind speed gradients that can be found along the coastline, and WW3 simulations driven by the downscaled WRF produce better bulk and spectral wave fields when compared to observations. Implications of the results for wind resource characterization are then discussed.

Acronyms and Abbreviations

CFS	Climate Forecast System
COARE	Coupled Ocean–Atmosphere Response Experiment
COAWST	Coupled Ocean–Atmosphere–Wave–Sediment–Transport Modeling System
DOE	Department of Energy
ERA5	The European Centre for Medium-Range Weather Forecasts Reanalysis v5
MERRA-2	The second Modern-Era Retrospective analysis for Research and Applications
MYNN	Mellor-Yamada-Nakanishi-Niino
NDBC	National Data Buoy Center
NOAA	National Oceanic and Atmospheric Administration
PBL	Planetary Boundary Layer
PNNL	Pacific Northwest National Laboratory
RAP	Rapid Refresh
RMSE	Root-Mean-Squared-Error
SST	Sea Surface Temperature
WRF	Weather Research and Forecasting
WW3	WAVEWATCHIII
YSU	Yonsei University

Contents

Figures

Tables

1.0 Introduction

As the U.S. and the world aim to reduce greenhouse gas emissions, wind energy development will be of vital importance. Offshore wind energy is less developed than onshore wind energy, especially in the U.S., but has the advantage of potentially larger and more reliable wind resource. The first large-scale offshore wind farm in the nation recently began operation off the U.S. Atlantic Coast (https://www.mass.gov/news/vineyard-wind-americas-first-large-scale-offshore-wind-farm-delivers-full-power-from-5-turbines-to-the-new-england-grid). In this region, the water depths are generally shallow enough (< 60 m) such that fixed-bottom monopiles may be used in construction (Musial et al. 2021).Off the U.S. Pacific coast, two wind energy areas have been designated by the Bureau of Ocean Energy Management off the coast of California (Krishnamurthy et al. 2023), one near Humboldt County in northern CA, the other near Morro Bay in central CA. However, for the U.S. Pacific Coast, water depths increase rapidly with distance from shore, such that the development of floating wind turbine technology will be required to take advantage of this resource. This makes it all the more critical to have accurate assessments of wind resource in specific U.S. Pacific offshore regions prior to an expensive deployment.

One tool that has been used to assess this resource is the fleet of Department of Energy (DOE) lidar buoys, which Pacific Northwest National Laboratory (PNNL) has been deploying on behalf of the Bureau of Ocean Energy Management since 2014 (Shaw et al. 2020; Krishnamurthy et al. 2023). In addition to a suite of standard meteorological and oceanic measurements, the buoys are equipped with a Doppler lidar that permits nearly continuous, year-round measurements of wind speed at various range gates in the boundary layer, including near the heights relevant to wind turbine applications (i.e., about 100 m above the surface).The initial deployment took place off the U.S. Atlantic Coast, with one buoy each near Virginia and New Jersey approximately 40 km and 5 km offshore, respectively. The buoy measurements provided an opportunity to evaluate the skill of standard atmospheric analysis / reanalysis products in predicting offshore hub-height wind speed across the deployment period (Sheridan et al. 2020; Sheridan et al. 2021). It was found that all products had negative wind speed biases, but that the higher resolution products such as the 13-km Rapid Refresh (RAP; Benjamin et al. 2016) had somewhat better observational / model correlations than the other products.

A number of factors could be responsible for offshore hub-height wind speed model errors. Insufficient model resolution, both horizontal and vertical, seem likely to be a factor. The relative scarcity of data in the offshore environment, which hinders improving forecast skill via data assimilation, is likely another factor. Additionally, specific to the offshore environment, misrepresenting the interaction processes between the atmosphere and the ocean can be a source of model error. For example, Monin-Obukhov similarity theory (Edson and Fairall 1998) is generally used in atmospheric models to determine the surface layer wind speed profile and surface heat, moisture, and momentum fluxes, and is a function of the surface roughness length. However, over the ocean, the roughness length is a function of the surface wave state, which is generally not a predictive field in atmospheric models.

To investigate sources of offshore hub-height wind speed model error in more detail, Gaudet et al. (2022) performed in-house simulations of cases from the East Coast buoy deployment period that exhibited large errors when compared to reanalysis products, and evaluated the simulations against the Virginia and New Jersey lidar buoy data. The simulations used the Coupled Ocean–Atmosphere–Wave–Sediment–Transport (COAWST) Modeling System (Warner et al. 2010), a freely available package developed at Woods Hole Oceanographic Institute which can mutually

couple explicit atmospheric, wave, oceanic, and sediment transport models. For tropical cyclone and cold frontal cases, the benefits of kilometer-scale resolution (in this case, 5 km) on model biases and correlations were shown. A comparison was performed between an atmosphere-only simulation, a two-way coupled atmosphere-wave simulation, and a one-way coupled simulation where atmospheric roughness was determined from an offline wave model simulation. The experiments showed for the above cases that the two-way coupled simulation had the best wind speed correlation statistics at buoy level (4 m) and mitigated a systematic negative wind speed bias introduced in the one-way coupled simulations. Changes in hub-height wind speed predictive skill was less clear, but the general sensitivity of wind speed to wave-based roughness could be as high as 10% in stable conditions, and was present at hub height as well as buoy level.

After the West Coast deployment, similar studies were performed using the buoy data. There are a number of differences between the U.S. East Coast and West Coast offshore environments that make it unclear how the results of one region would apply to the other. The deeper bathymetry off the U.S. West Coast leads to different dynamics for longer-period waves. The region is frequently impacted by long-period swell waves that may be arriving from distant locations and have little relation to the local wind field. Meteorologically, the presence of an irregular coastline, in conjunction with steep topography, can lead strong along-coast flows whose impacts can reach tens of kilometers offshore. In the winter season the region can see landfalling extratropical cyclones including atmospheric rivers as well as downslope Santa Ana and Sundowner events; the summer season is dominated by northerly flow and low-level jets, and frequent low cloudiness.

Sheridan et al. (2022) performed an analysis of the West Coast Humboldt and Morro Bay lidar buoy hub-height wind speeds and used them to evaluate a suite of wind speed analysis / reanalysis products in the region. It was again found that the products on average underestimated hub-height wind speed, and that the highest resolution product had the best correlation statistics. However, the bias statistics for different reanalysis products varied widely depending on buoy location. As a general tendency, model biases tended to be more positive from noon to midnight, and summer through early fall; negative biases tended to prevail at other times.

In this study we perform atmosphere / wave-coupled simulations for two cases selected from the West Coast buoy deployment period characterized by large hub-height wind speed model errors, following the procedure of Gaudet et al. (2022) for the East Coast deployment. One is a cold season case around the Morro Bay deployment, while the other is a warm season case around the Humboldt deployment.

2.0 Background

2.1 U.S. Department of Energy Lidar Buoys

Details about the DOE lidar buoys and their deployment off the U.S. West Coast can be found in Sheridan et al. (2022) and Krishnamurthy et al. (2023). They were operated by PNNL in two locations designated as wind energy lease areas of the CA coast, one approximately 50 km off of Morro Bay in central CA (1100 m water depth), while the other was approximately 40 km west of Humboldt in northern CA (625 m water depth). The Morro Bay buoy was deployed from Sep 2020 to Oct 2021. The Humboldt buoy was initially deployed in Oct 2020, but a large wave event in Dec 2020 damaged the buoy, and it could not be redeployed until May 2021. The Humboldt buoy deployment was subsequently extended until Jun 2022.

The DOE lidar buoys were procured as AXYS WindSentinel™ buoys (Newsom 2016), but for the West Coast deployment were outfitted with Leosphere WindCube v2 lidar systems that can provide wind profiles from 40 m to 250 m above the surface. The buoys also include cup-and-vane and sonic anemometers to record wind speeds at buoy height (about 4 m above the surface), as well as temperature / humidity sensors, directional wave sensors, sea surface temperatures, conductivity, acoustic Doppler current profilers, and a pyranometer to measure downwelling shortwave radiation.

2.2 Wave Roughness Height

Since waves are not generally explicitly predicted by atmospheric models, the roughness length over water is typically parameterized from atmospheric fields near the surface. Generally, young growing waves move slower than the near-surface wind speed and act as roughness elements with respect to it (Smith et al. 1992). Over the open deep ocean, eventually longer-wavelength, higher-speed modes develop, which contribute little to the roughness, and can propagate away from the source region as swell. Historically, in fully developed sea the wave-based roughness has been taken to be simply proportional to the wind stress (Charnock 1995); since in atmospheric models the roughness length is used in turn used to derive the wind stress from Monin-Obukhov similarity theory, an iterative method to derive both is required. The Coupled Ocean–Atmosphere Response Experiment (COARE) series of algorithms, including those to derive roughness length and wind stress, take this general approach, but have the Charnock proportionality factor be a function of wind speed (Fairall et al. 2003; Edson et al. 2013).

An additional potential shortcoming to these parameterizations is that they may not apply to young wave age states; a variety of roughness parameterizations have been developed to include this dependence (Oost et al. 2002; Drennan et al. 2005; Edson et al. 2013; Sauvage et al. 2023). Furthermore, over regions with shallow depths, not only can waves increase in height through shoaling, but the phase speed is capped at the shallow-water speed, potentially allowing all modes to act as roughness elements (Smith et al. 1992). Neglecting these effects can lead to systematic biases in predicted offshore wind speed over shallow coastal waters (Jiménez and Dudhia 2018). However, including these effects in atmospheric models is hindered by the implied need to have some wave state predictive capability within the model.

The Taylor and Yelland (2001) parameterization is another wave-roughness parameterization, and is the one used in this study. Here roughness, z_0, is given by:

$$z_0 = 1200\, H_s \left(\frac{H_s}{L_p}\right)^{4.5} \quad (1)$$

with units of meters. This is a function of two bulk properties of the wave field: significant wave height (H_s), and wavelength of the peak wave period (L_p). One feature of this parameterization is that it is not a function of either the wind stress or wind velocity, and so is a function of wave state only. In this study we use two-way coupled atmosphere / wave simulations to ensure predicted wave state is available to the roughness parameterization in the atmospheric model.

2.3 Modeling Systems

2.3.1 COAWST Modeling System

To perform the coupled simulations, we used version 3.6 of the Coupled Ocean–Atmosphere–Wave–Sediment–Transport (COAWST) Modeling System (Warner et al. 2010) developed at Woods Hole Oceanographic Institute. This is a wrapper that allows atmospheric, wave, oceanic, and sediment transport models to all mutually interact with each other (Figure 1) through the use of the Model Coupling Toolkit, and an adapted version of the Spherical Coordinate Remapping Interpolation Package (Jones 1998) to conservatively remap fields between the different grids used by the model components. We used mostly the same code and configuration (Weather Research and Forecasting (WRF) atmospheric model (Skamarock et al. 2019) and WAVEWATCH III® (WW3) wave model (The WAVEWATCH III® Development Group 2019)) as was used in the Gaudet et al. (2022) study for the U.S. East Coast, but with features specific to the West Coast application as described below.

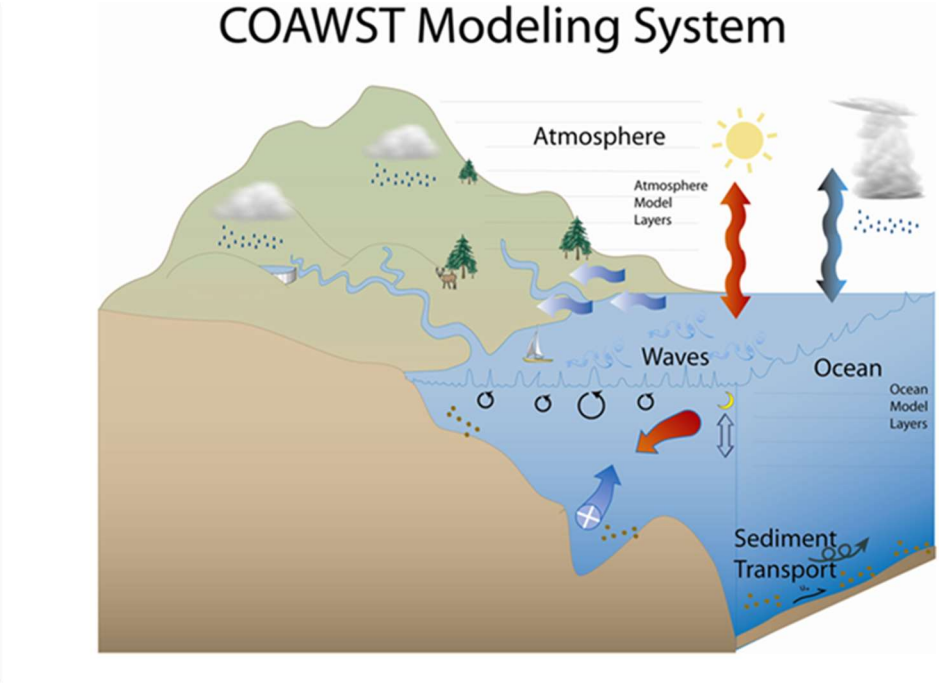

Figure 1. Diagram showing processes captured in COAWST modeling framework. Adapted from Warner et al. (2010).

2.3.2 WRF

We used the WRF version 4.0.3 as provided within COAWST for both stand-alone atmospheric and wave-coupled simulations. The physics configuration is based on that of Gaudet et al. (2022), with important features given in Table 1. More details on the configuration can be found in Gaudet et al. (2022), but we note some key differences from that study below.

Table 1. List of key configuration parameters for WRF simulations used in this study.

WRF Namelist Option	Value
Horizontal Dimensions	180 x 160, 202 x 352
Horizontal Grid Spacing (km)	9, 3
Vertical Dimension	72
Timestep (s)	30, 10
Boundary Layer Parameterization	Yonsei University (YSU)
Microphysics	WSM 6 Class
Radiation	RRTMG
Convective Parameterization	Kain-Fritsch
Land Surface Model	Noah
Data Assimilation	Above-boundary-layer analysis nudging (Grid 1 only)

One difference from Gaudet et al. (2021) is that the boundary layer parameterization used was the Yonsei University (YSU) scheme (Hong et al. 2006) instead of the Mellor-Yamada-Nakanishi-Niino (MYNN) scheme (Nakanishi and Niino 2009). This was based on studies that suggested the YSU scheme had reduced wind speed biases off the U.S. West Coast compared to the MYNN (Liu et al. 2024).

For the stand-alone WRF simulation, oceanic roughness is parameterized as a function of wind speed, according to the COARE 3.0 parameterization (Fairall et al. 2003). While this parameterization is implemented in the surface layer scheme associated with MYNN, it is not present by default for the YSU surface scheme; therefore, the YSU surface layer scheme was modified to make this the case.

As in Gaudet et al. (2022), meteorological and sea surface temperature (SST) initial and boundary conditions are derived from the Climate Forecast System version 2 (CFSv2; Saha et al. 2010; Saha et al. 2014), which includes intermittent data assimilation of coupled atmosphere/land/ocean models into a variant of the standard Global Forecast System weather prediction model (standard fields at 0.5 degree horizontal grid spacing, surface fields at 0.2 degrees). Advantages of using CFSv2 for this application include its global extent, high temporal resolution (every hour), and use of ocean model output.

Our WRF grid configuration is shown in Figure 2. We used two nested grids of 9 km and 3 km grid spacing, with analysis nudging used to constrain the Domain 1 fields above the planetary boundary layer (PBL). Domain 2 was left unconstrained except for the lateral and surface

boundary conditions, which included 3-hr updates of the SST fields from the CFSv2 analysis. All subsequent analysis in this report will be for the 3-km Domain 2.

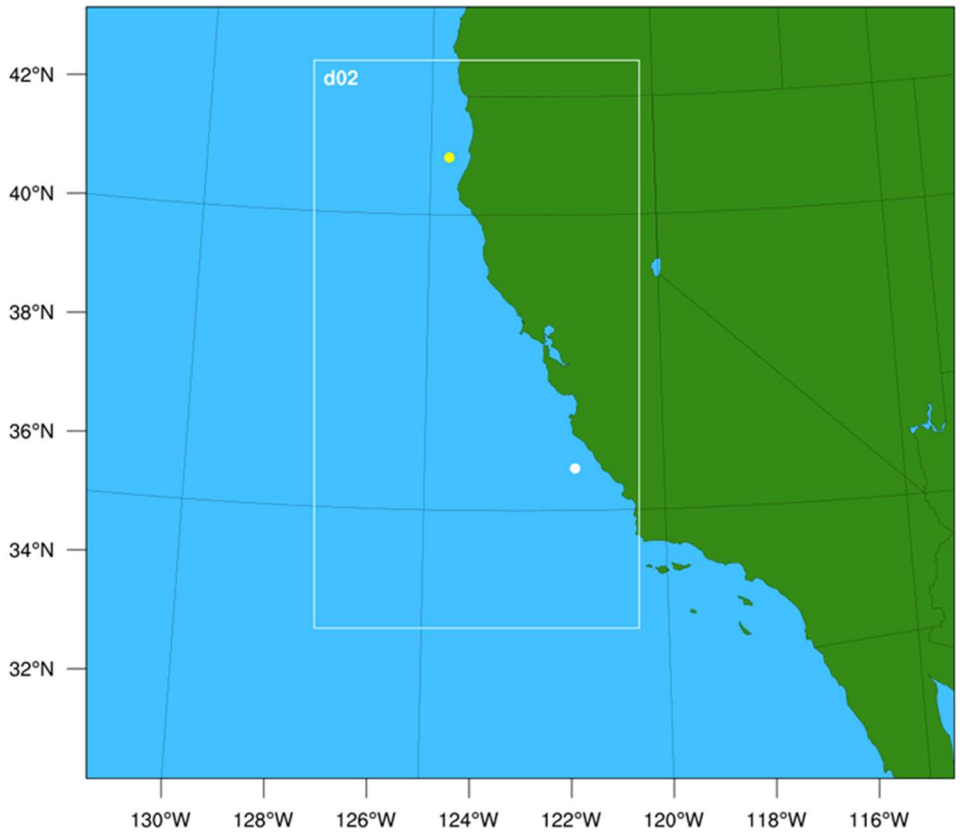

Figure 2. Domain configuration for all WRF simulations performed in this study. Locations of the Morro Bay (white) and Humboldt (yellow) lidar buoys are shown.

We use the Taylor and Yelland (2001) parameterization to relate oceanic roughness height to wave field parameters. However, we make two modifications to the scheme. One, instead of using the peak wavelength, we use the mean wavelength of the wave spectrum (i.e., the wavelength corresponding to the mean frequency of the spectrum). In this we follow Sauvage et al. (2023), who provided two justifications. 1) The mean wavelength is a more robust parameter than peak wavelength, e.g., small changes to a bimodal spectrum may cause the peak wavelength to oscillate between two widely different values. 2) Measurements suggest that in mixed sea, the wave stress is more reflective of higher frequency wind waves than lower frequency swell, and typically the mean wavelength will have higher frequencies / shorter wavelengths than the peak wavelength. The second modification, which is typical for model applications, is that we add an additional term that is based on the roughness of a water surface in laminar conditions, and is a function of surface momentum stress and the air viscosity. This term effectively provides a lower bound for the roughness length in conditions with little or no wave presence.

2.3.3 WW3

We wanted to compare output from a two-way WRF / WW3 coupled simulation to one-way coupled simulations, in which stand-alone WW3 simulations provide wave information to WRF

simulations, and separate simulations in which stand-alone WRF simulations provide wind information to WW3. Toward this end, a stand-alone WW3 simulation was performed over the time period of the buoy deployment prior to the performance of any COAWST simulations, so that its development could help guide the design of the latter.

The third-generation, phase-averaged WW3 model v6.0.7 was used to dynamically downscale the waves reaching California (Figure 3). To account for the distant swells, the National Oceanic and Atmospheric Administration (NOAA) global wave model was reimplemented as part of the modeling system. This model has a 0.5 arc-degree resolution. The two intermediate models have a resolution of 10 arc-minutes and cover the Central Pacific Islands and the U.S. West Coast, based on the source regions of wave energy to the lidar buoy deployment using the ESTELA method (Pérez et al. 2014) and a global wave hindcast (Wu et al. 2020). The latter model extends from Baja California, Mexico to northern Vancouver Island, British Columbia, Canada. The model coverage is shown in Figure 3. Finally, a third model offshore California was developed. This model has a spatial resolution of 3 km and extends from 28°N to 45°N and from 132°W to the coastline. All models are referenced to WGS84 and the bathymetry is interpolated from ETOPO 1 (Amante and Eakins 2009). This domain is the one that will provide the wave state for the one-way coupled WRF / WW3 coupled simulations. To minimize inconsistency issues, the extent of the 3-km WW3 was designed to be large enough to encompass both the 9-km and 3-km WRF domains.

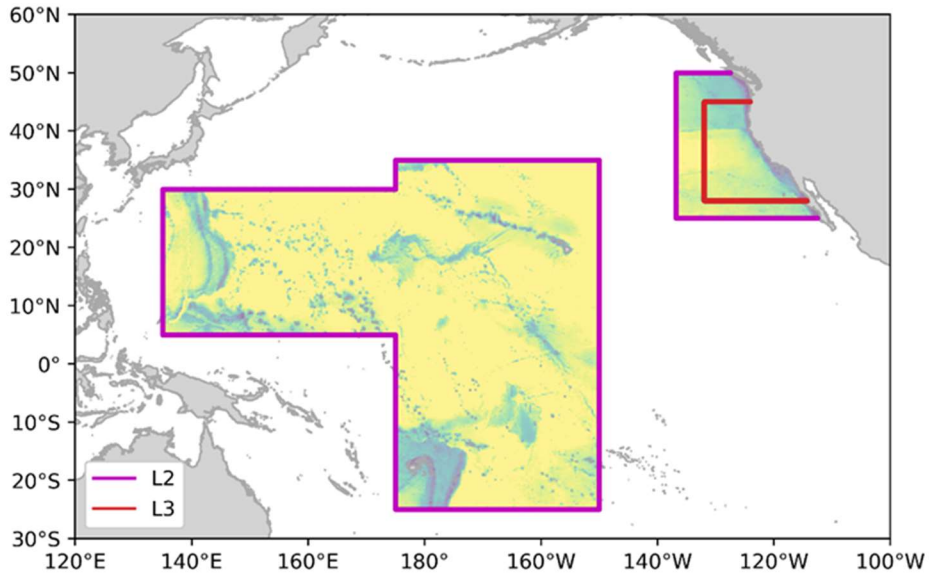

Figure 3. Domain configuration used for the stand-alone WW3 simulations performed for this study. Two nested levels L2 (magenta) and L3 (red) are shown (L1 is global).

WW3 solves the wave action equation as a function of time, position, frequency, and direction. Wave growth and dissipation due to whitecapping are modeled with the ST4 source term package (Ardhuin et al. 2010). Swell dissipation is considered as part of the ST4 package. This source term package has been successfully implemented in global coastal hindcasts (Pérez et

al. 2017), extreme weather events in the U.S. West Coast (Ellenson and Özkan-Haller 2018), and the U.S. East Coast at the lidar buoy deployments (García Medina et al. 2020; Gaudet et al. 2022); among many others. Wind growth intensity and swell dissipation are the parameters tuned to reduce model errors. Additional source terms included in the model are non-linear quadruplet interactions (S_{nl}; Hasselmann et al. 1985), dissipation due to bottom friction (S_{bot}; Hasselmann et al. 1973), and depth-induced breaking (S_{brk}; Batties and Janssen 1978). Default parameters and formulations were used for these source terms. The wave spectrum was discretized with 34 frequencies spaced logarithmically with a 1.1 increment factor providing coverage from 0.03 to 0.6968 Hz. The spectrum is divided into 36 equally spaced directions with the time explicit solution implemented. The global time step ($\mathbf{\Delta t}_{\boldsymbol{g}}$), spatial propagation time step ($\mathbf{\Delta t}_{\boldsymbol{\lambda,\phi}}$), maximum refraction and wavenumber shift time step ($\mathbf{\Delta t}_{\boldsymbol{k}}$), and the dynamical source term integration time step ($\mathbf{\Delta t}_{\boldsymbol{s}}$) are given in Table 2.

Table 2. WW3 model time steps

Model	Level	Agency	$\Delta t_g\ [s]$	$\Delta t_{\lambda,\phi}\ [s]$	$\Delta t_k\ [s]$	$\Delta t_s\ [s]$
Global	L1	NOAA	1800	600	900	30
Central Pacific	L2	PNNL	300	300	150	10
West Coast	L2	NOAA/PNNL	900	450	450	15
California	L3	PNNL	50	50	25	10

The model is forced by analyzed and short term forecast global winds at 10 m height from CFSv2, which is used in the initial and boundary conditions for the WRF simulations. The wind fields are provided at a 1-hour interval.

3.0 Baseline Model Development

3.1 Wave Model

As an initial step, the WW3 model was calibrated in a baseline configuration, based on significant wave height and swell wave height error statistics.

The multimodal sea state of California requires that the model performs well in predicting swell and locally generated waves. The wind growth can be tuned by modifying the non-dimensional growth parameter (β_{max}) in the source term equation:

$$S_{in} = \frac{\rho_a}{\rho_w}\frac{\beta_{max}}{\kappa^2} e^Z Z^4 \left(\frac{u_*}{C}\right)^2 \times \max[\cos(\theta - \theta_u), 0]^p \, \sigma F(k,\theta) \quad (2)$$

where ρ_a and ρ_w are the density of the air and water, respectively, κ is the von Kármán constant; Z is the effective wave age; u_* is the wind friction velocity; θ is the wave direction; θ_u is the wind direction; and F is the wavenumber-direction spectrum. Growth parameters in the range of 1.2 to 2.0 have been found to minimize errors in different applications (Rascle and Ardhuin 2013; Mentaschi et al. 2015; Perez et al. 2017; Shaw et al. 2020). Stopa (2018) implemented a global WW3 model with ST4 physics and found that the optimal β_{max} when using the CFS reanalysis is 1.385 when comparing against satellite derived measurements. Calibration of this parameter assesses the wave growth everywhere in the domain. To constrain swell growth and mitigate errors due to non-linear transfer of energy the swell dissipation due to turbulence $(S_{out,tur})$ is adjusted via the tunning parameter (s_1) in Equation (4):

$$S_{out,tur} = -\frac{\rho_a}{\rho_w}\left[\frac{16 f_e \sigma^2 u_{orb}}{g}\right] N \quad (3)$$

$$f_e = s_1 f_{e,GM} + [|s_3| + s_2 \cos(\theta - \theta_u)]\frac{u_*}{u_{orb}} \quad (4)$$

where u_{orb} is the wave orbital velocity, σ is the radian wave frequency, and g is the acceleration due to gravity. Default values are used for parameters s_3 and s_2. Parameter s_1 has been tuned in the range of 0.66 (default) to 0.80 (The WAVEWATCH III® Development Group 2019).

Model calibration was performed in the period from 1 January 2021 to 30 April 2021 using the CFSv2 forcing. During this period both lidar buoys were active and several winter storms approached the region. In addition, the global ensemble consisting of L1 and L2 was calibrated independently to the L3 model. The reason for this is because the L3 model will be executed independently of the L1-L2 ensemble as part of a coupled model system in future tasks of this project.

The wave spectrum was divided into swells and local wind seas using a 10 s frequency cutoff to analyze the effect of calibration on the prediction of both components of the wave spectrum. First, the calibration process targeted the reduction of errors in the prediction of swells in the L1-L2 model ensemble. Then, a separate model calibration was performed in the L3 model which was executed independently of the L1-L2 model and forced by time varying wave spectra at every open boundary node collected from the L1-L2 model execution.

The target buoys used for calibration were ones maintained by the National Data Buoy Center (NDBC), which typically record wave spectral and bulk parameters as well as buoy-level meteorological fields and sea surface temperature. We made use of NDBC buoy 46028 which is located around 5 km from the Morro deployment and buoy 46022 located around 15 km from the Humboldt deployment. At the time when these simulations were performed the wave spectra had not been downloaded from the data cards onboard the lidar buoys. The wave spectra are needed to perform the calibration to swells and wind seas depending on the model being evaluated.

3.1.1 Global and Regional Models (L1 and L2)

A combination of β_{max} = 1.33 and a swell dissipation factor s_1 = 0.80 minimizes the swell wave height bias magnitude at the two call sites (Figure 4). Not surprisingly bias increases linearly with increasing β_{max} and decreases with increasing s_1. The combination that minimizes swell bias also minimizes the swell prediction root-mean-squared error (RMSE), with similar values to s_1 = 0.73. Biases in the total sea state with the β_{max} = 1.33 and s_1 = 0.80 show the most underprediction, however, which indicates that locally generated waves are underpredicted with this configuration. This can be addressed by separately calibrating the L3 model.

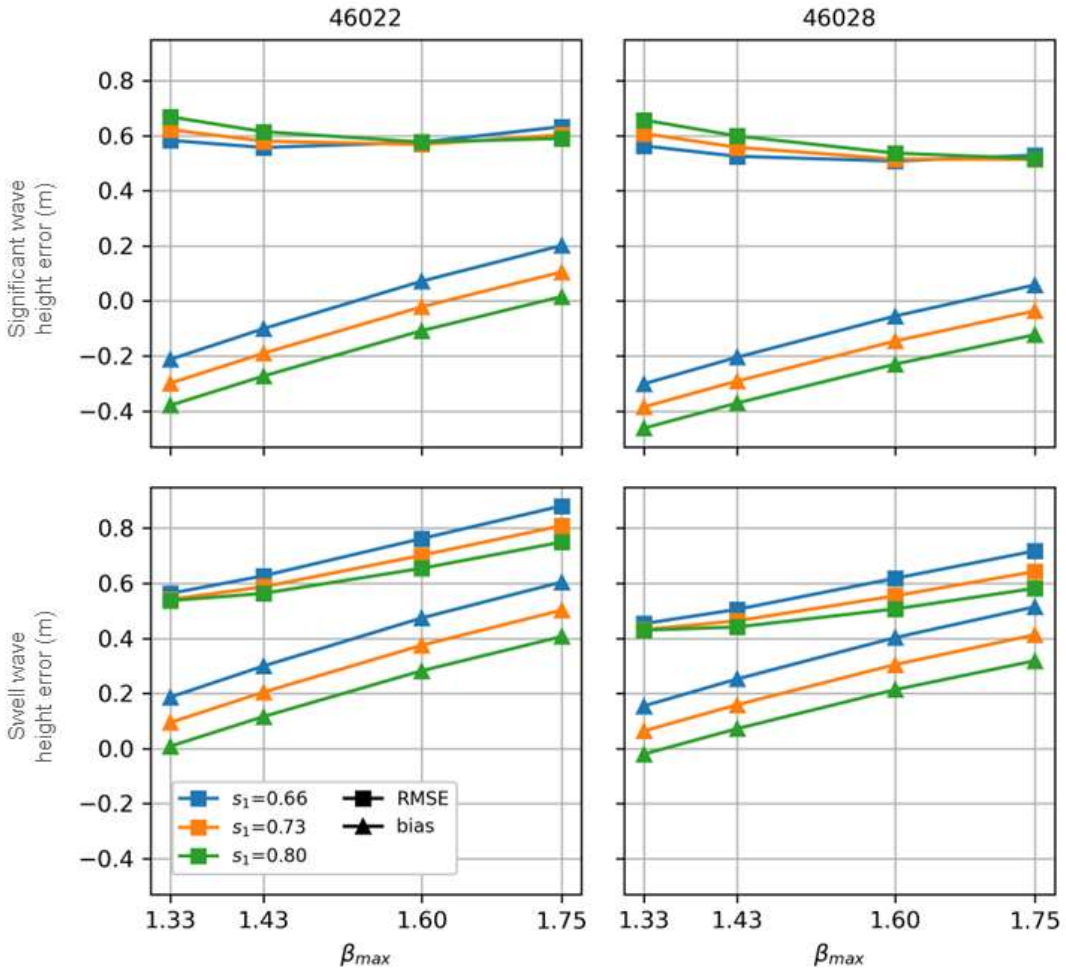

Figure 4. Errors in significant wave height (top row) and swell wave height (bottom row) prediction between 1 January and 30 April 2021 at 46022 (left) and 46028 (right).

3.1.2 California Model (L3)

The California model is executed with spectral boundary conditions from the L1-L2 ensemble. Model simulation results exclude a 14 day spin up period to allow for waves to cross from the boundary to the shore. The calibration period for the L3 model coincides with the L1-L2 ensemble. Four simulations were performed varying β_{max} from 1.33 to 1.75 and the default swell dissipation factor s_1 = 0.66. RMSE and bias shown in Figure 5 are calculated at 46022 and 46028. It was found that the error in predicting the total sea state and wind seas was reduced with increasing β_{max}. Total sea-state RMSE errors are smaller than those found with the global ensemble (compare Figure 4 and Figure 5). Swell errors show an increasing trend with increasing β_{max} to 1.75 but remained below the default model configuration (β_{max} = 1.33, s_1 = 0.66). Subsequent simulations of the L3 model domain, including those within the two-way coupled COAWST simulations, thus use (β_{max} = 1.75, s_1 = 0.66).

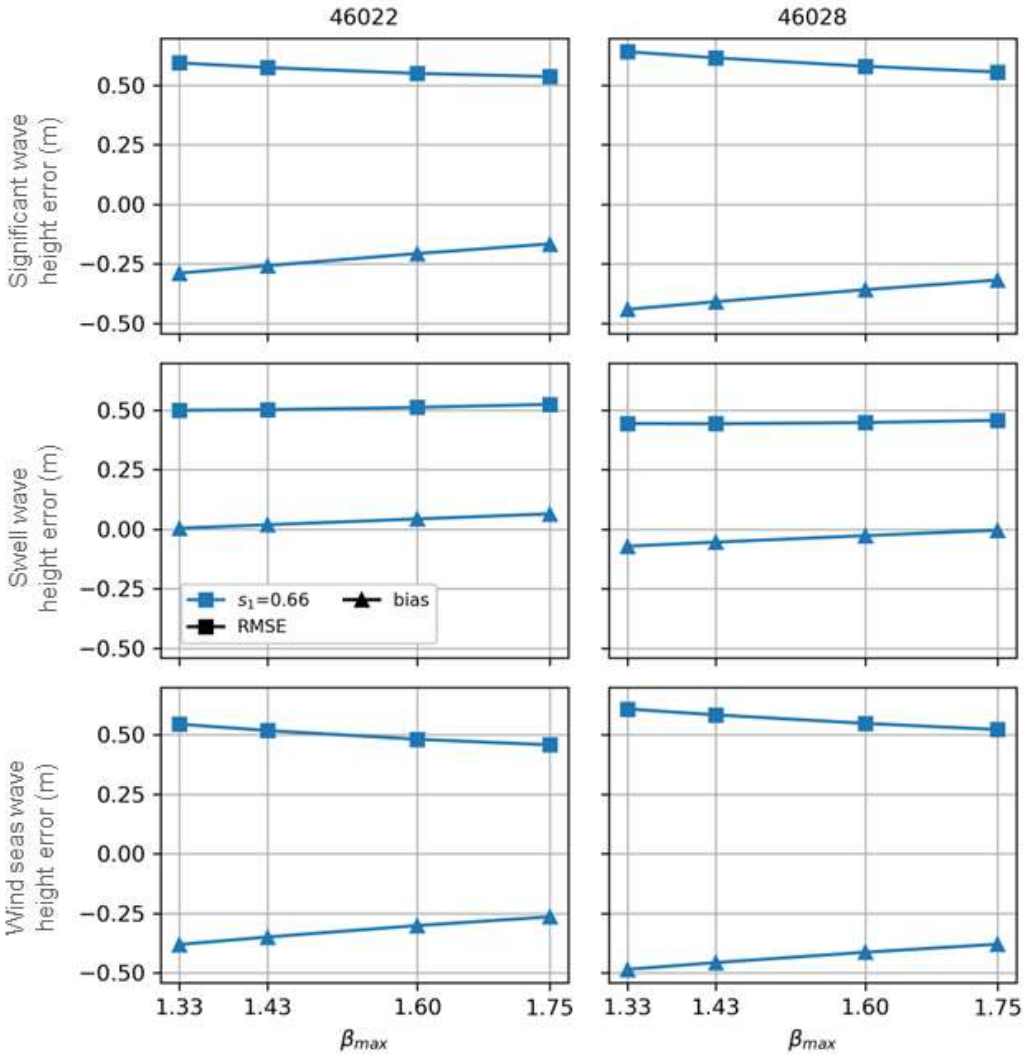

Figure 5. Errors in significant wave height (top row), swell wave height (middle row), and wind seas wave height (bottom row) prediction between 1 January and 30 April 2021 at 46022 (left) and 46028 (right) from the L3 model.

4.0 Experimental Design

The experimental procedure was similar to what was used in Gaudet et al. (2022). During the lidar buoy deployment periods we selected cases for which large errors in hub-height wind speeds were apparent among existing reanalysis products (including the CFSv2, RAP, the second Modern-Era Retrospective analysis for Research and Applications (MERRA-2; Gelaro et al. 2017), and the European Centre for Medium-Range Weather Forecasts (ECMWF) Reanalysis v5 (ERA5) (Hersbach et al. 2020)), and for which observational data was available. The cases were then simulated with the COAWST modeling system using different modes of model coupling. We focused on hub-height wind speed prediction by the atmospheric model (WRF) in three modes of coupling with the wave model (WW3): stand-alone WRF; one-way coupled WRF, for which WRF received wave information from the stand-alone WW3 simulation described in Section 2.3.3; and two-way coupled WRF, for which WRF and WW3 are run in unison and exchange information for the duration of the simulation (Figure 6).

Initial comparisons between the wave fields of the two-way coupled simulation and those from the stand-alone WW3 simulation suggested that it generally took about 18-36 hours to fully spin up the wave field in the two-way coupled simulation. Because of this, for the final set of two-way coupled simulations, the initialization time was moved backward so that a 24-hour spin up period was permitted, and discarded for further analysis.

In addition to the suite of WRF simulations, additional simulations were performed for which WW3 was run in stand-alone mode, but driven by winds derived from the two-way coupled WRF simulation. Analysis of WW3 wave fields were then performed on the stand-alone WW3 simulation, two-way coupled simulation, and one-way coupled, WRF-driven WW3 simulation.

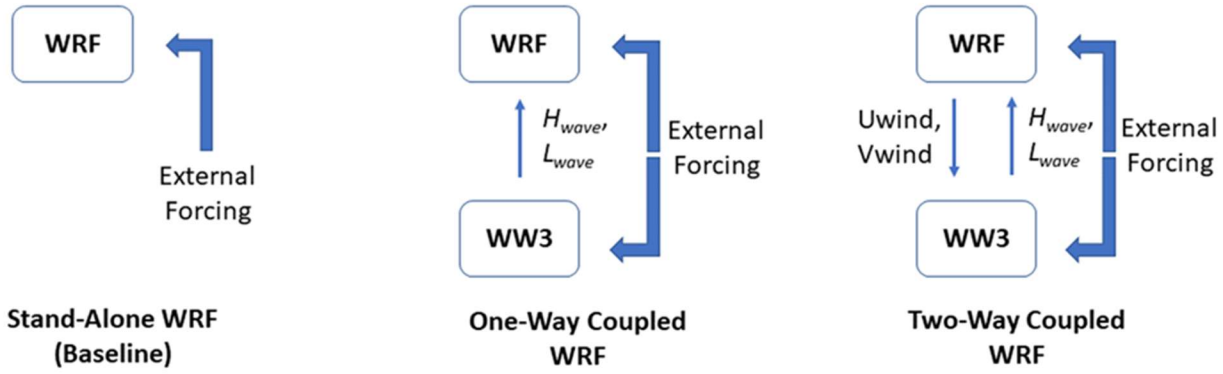

Figure 6. Description of WRF / WW3 interaction for stand-alone WRF, one-way coupled WRF, and two-way coupled WRF. Adapted from Gaudet et al. 2022.

5.0 Results

5.1 Case of 11 Feb 2021

The case of 11 Feb 2021 was associated with a cold frontal passage on the U.S. West Coast. The morning of 11 Feb, northwesterly flow associated with offshore high pressure was beginning to transition to southwesterly in advance of the frontal system (Figure 7). Shortly after 00 UTC on 12 Feb 2021, winds at Morro Bay begin veering, becoming southwest by 06 UTC. Associated with the cold front passage at Morro Bay is a shift to northwest winds and a sharp peak in wind speed, followed by a sustained period of elevated winds (Figure 8). While most available reanalysis products handled the event reasonably well, they usually failed to reproduce the initial wind ramp.

A)

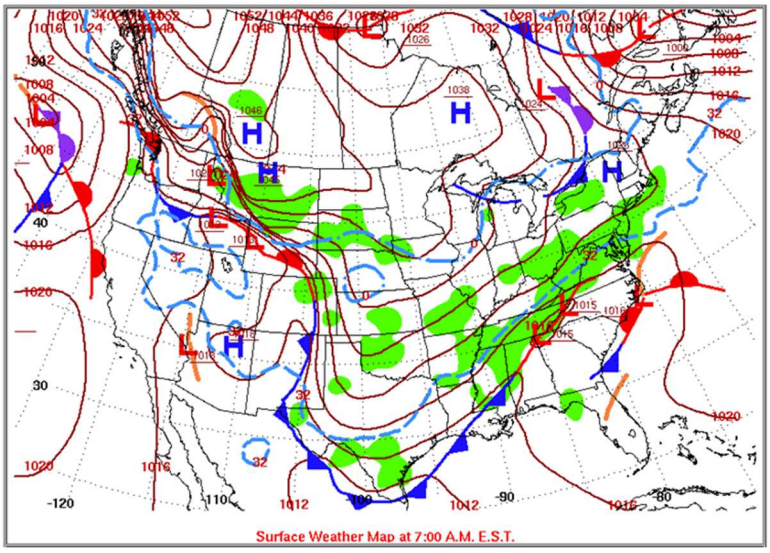

B)

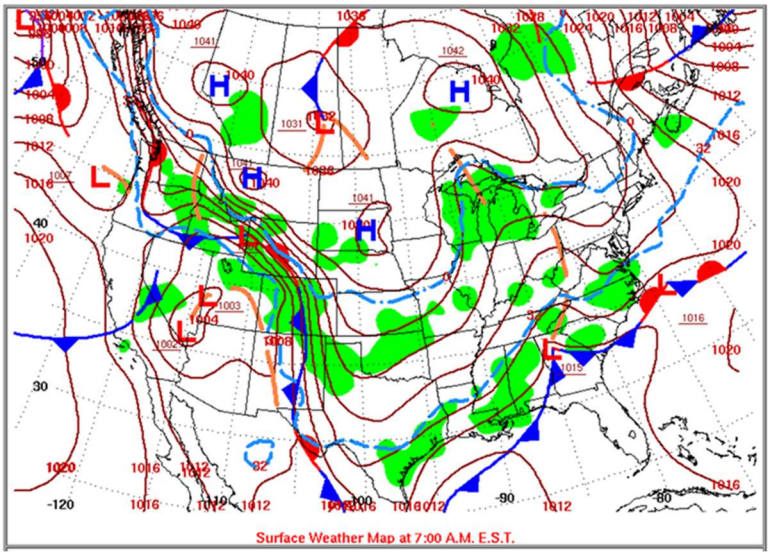

Figure 7. Synoptic weather maps for the mornings of 11 Feb 2021 (a) and 12 Feb 2021 (b). Courtesy National Centers for Environmental Prediction Weather Prediction Center.

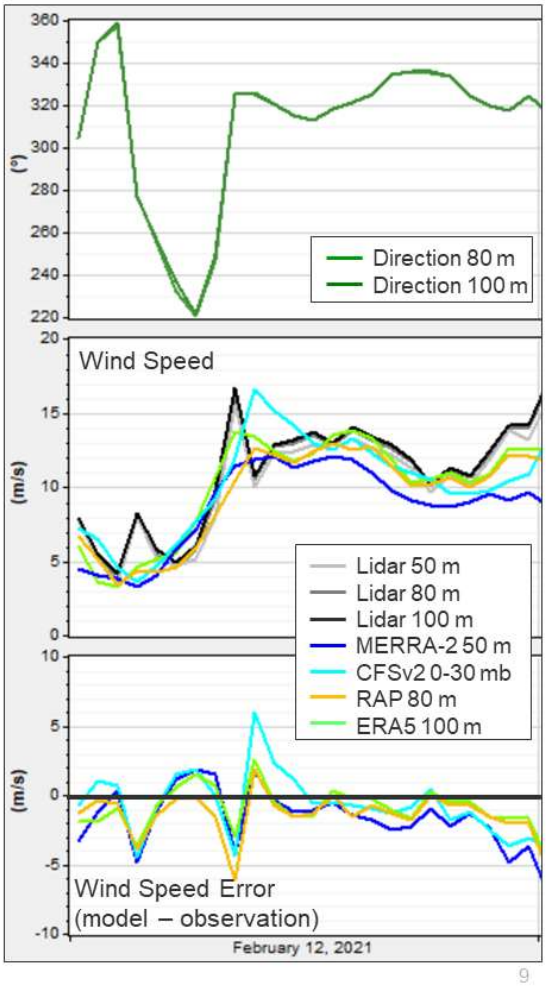

Figure 8. (Top) Time series of 100-m wind direction observed at the Morro Bay lidar buoy. (Middle) Time series of 100-m wind speed at Morro Bay location observed at lidar buoy (black) and for different reanalysis products (colored, labels given in figure). (Bottom) Time series of 100-m wind speed errors relative to Morro Bay lidar buoy.

We began the WRF simulations for this case at 12 UTC on 10 Feb 2021, extending for 60 hours, and to allow for model spin up, only focusing on the time period after simulation hour 24. A comparison between the baseline, one-way coupled, and two-way coupled 100-m wind speeds is shown in Figure 9, along with data from the lidar buoy stationed at Morro Bay. (Unfortunately, a massive wave event took down the lidar buoy stationed at Humboldt in Dec 2020, and this event was during the period that the Humboldt buoy was inactive.) We see that all simulations predict the wind ramp associated with the frontal passage quite well, except for being approximately 1-2 hour late. The models are also somewhat too fast in wind speed prior to 00 UTC 12 Feb, then somewhat too slow until the frontal passage, then somewhat too fast immediately after the frontal passage, all by amounts in the range of 2-5 m/s.

Among the different WRF configurations, the range in wind speeds is quite small. Until about forecast hour 50, when there is a discernible difference, it is the two wave-coupled models that agree with the baseline as an outlier. For two such periods (before forecast hour 36, and around forecast hour 45), the biases of the baseline simulation are increased in the two wave-coupled

simulations, by 0.5 - 1.0 m/s. Clearly, however, this does not seem to be a case where wave coupling is having a large impact on model skill, at least at the Morro Bay buoy location.

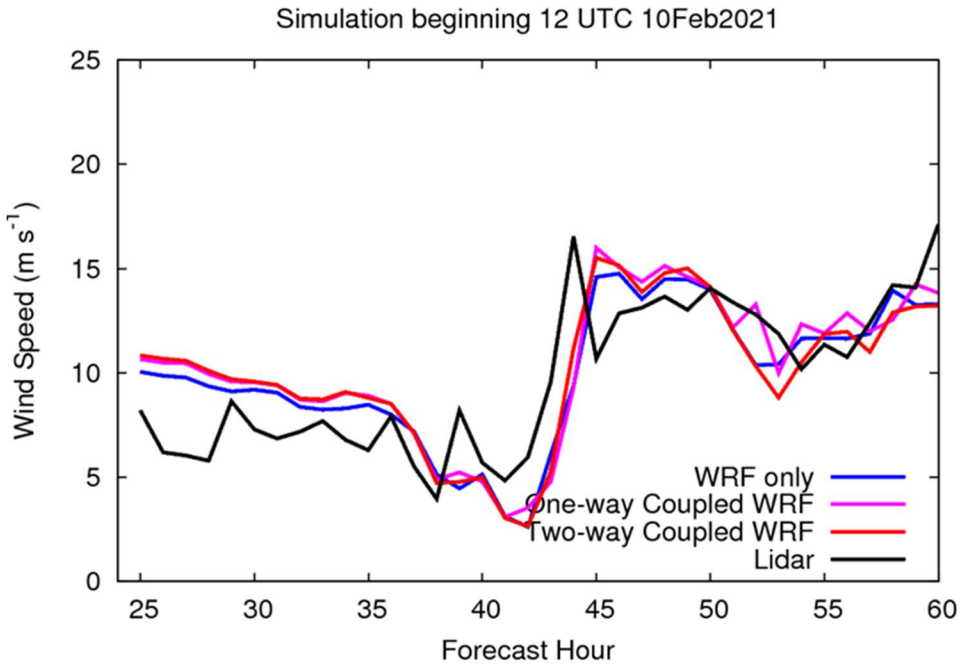

Figure 9. Time series of 100-m wind speed at Morro Bay during 11 Feb 2021 case for lidar buoy (black), stand-alone WRF (blue), one-way coupled WRF (magenta) and two-way coupled WRF (red). Only period after forecast hour 24 (12 UTC 11 Feb 2021) is shown.

However, to gain more insight into the role of wind / wave coupling on the model wind fields, we continue the analysis across the entire model domain. Figure 10 shows the 100 m wind field across the 3-km domain in the baseline simulation, and then the differences in wind speed between the one-way and two-way coupled simulations with the baseline. The top row is valid at 00 UTC 12 Feb, when northwesterly winds are still present at Morro Bay, but the approaching front can clearly be seen reaching the coast to the north near Point Arena. Both wave-coupled models have similar tendencies toward increased 100-m wind speeds throughout the pre-frontal region, by values on the order of 0.5 -- 1.0 m/s. However, in the pre-frontal region decreases in wave-induced wind perturbations tend to occur where the wind speed itself is smaller. Thus, including wave-based roughness seems to increase the pre-frontal spread of wind speeds, in the sense that higher wind speeds (> about 7 m/s) are increased, while lower wind speeds are reduced. In the post-frontal region, by contrast, there is more difference between the one-way and two-way coupled simulations; in the former, wind speeds are also increased, whereas in the latter the wind speeds are either little changed, or actually decreased in the two-way coupled simulation.

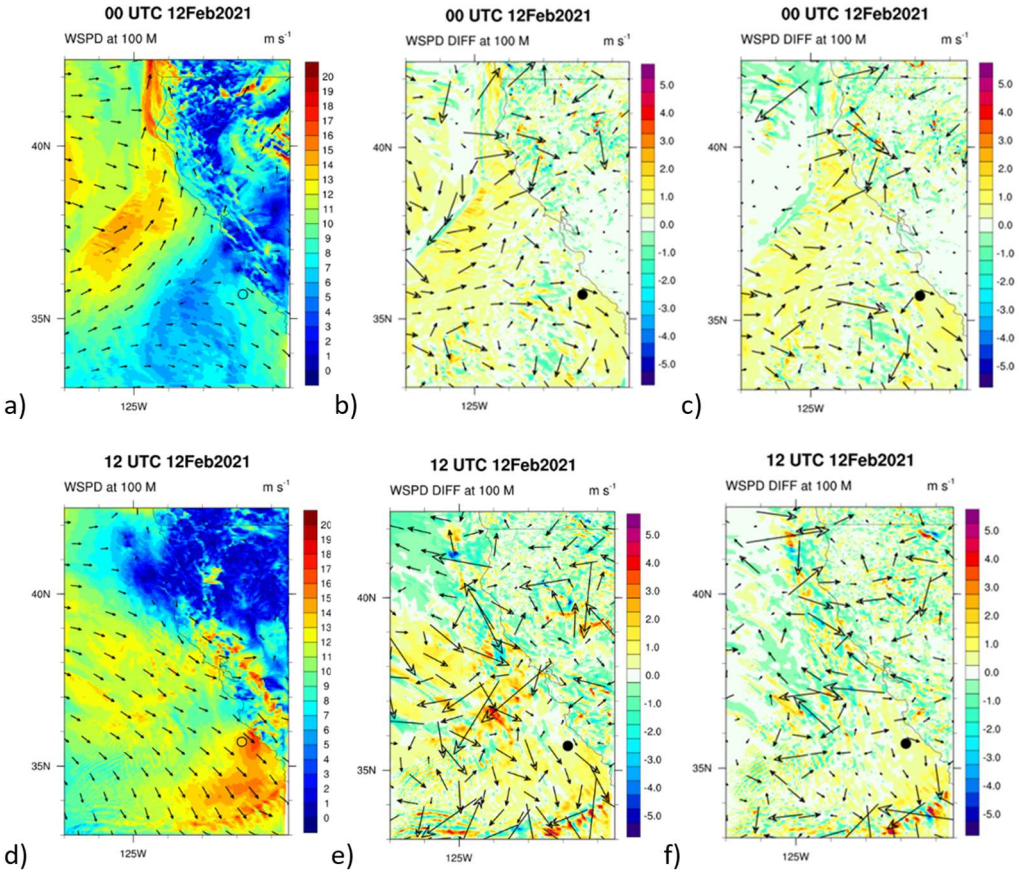

Figure 10. Simulated 100-m wind speed in stand-alone WRF simulation (a, d), and difference between simulated 100-m wind speed in one-way coupled (b, e) and two-way coupled (c, f) simulations from the stand-alone WRF simulation. Panels a-c are valid 00 UTC 12 Feb 2021; panels d-f are valid 12 UTC 12 Feb 2021. For panels a and d, location of and observed 100-m wind speed at location of the Morro Bay lidar buoy is indicated by circle according to the same color scale.

By 12 UTC 12 Feb, when the front has moved through the Morro Bay region (Figure 10, panels d-f), we still see in both wave-coupled simulations a general trend of increased wave-coupled winds for wind speeds > 7 m/s, as at Morro Bay and points to the southeast, along with decreased wave-coupled winds for wind speeds < 7 m/2, as in the Humboldt Bay region and points north. However, there is an intermediate region, west of the San Francisco Bay area, where wind speeds are increased in the one-way coupled simulation, but decreased in the two-way coupled simulation. We also can see, in the northwestern part of the domain, regions where two-way coupled wind speeds are little different from the baseline simulation, but reduced in the one-way coupled simulation.

To see how the wave fields might be producing these differences, we examine the wave-induced roughness heights (Figure 11). We focus on a time immediately after the frontal passage at Morro Bay (10 UTC 12 Feb) as well as 12 UTC 12 Feb. At 10 UTC the roughness height is somewhat higher at Morro Bay in the two-way coupled simulation than in the one-way coupled simulation, but in both cases the actual value is small, less than 0.0001 m. For reference, a typically assumed ocean roughness length is 0.0002 m (Golbazi and Archer 2019; Sheridan et al. 2020). However, somewhat higher roughnesses in the two-way coupled

simulation can be seen west of the San Francisco Bay area. There is also, in the far northwest part of the domain, a zone of very high roughness lengths in the one-way coupled simulation, in association with a low pressure off the Oregon Coast, which are not apparent in the two-way coupled simulation. The reason is not clear, but is likely due to differences in the low pressure meteorology between the CFSv2 analysis that drives the stand-alone WW3, vs. the WRF meteorology

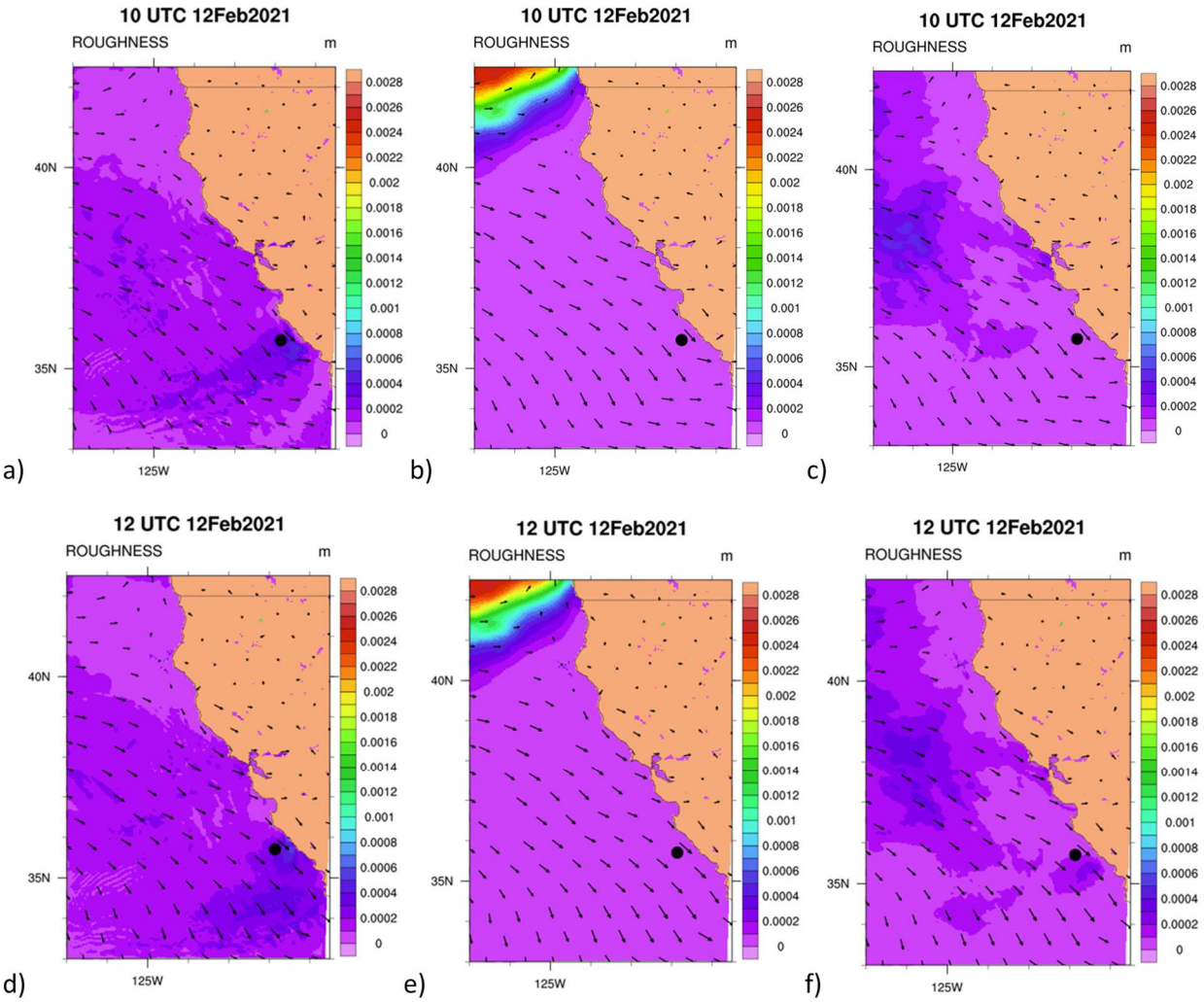

Figure 11. Simulated roughness height in stand-alone WRF simulation (a, d), one-way coupled WRF (b, e), and two-way coupled WRF (c, f) simulations. Panels a-c are valid 10 UTC 12 Feb 2021; panels d-f are valid 12 UTC 12 Feb 2021. Location of Morro Bay lidar buoy is indicated by circle.

At 12 UTC 12 Feb, the patterns are generally similar, but now the roughness is somewhat increased in the vicinity of the Morro Bay buoy. The larger roughness west of the San Francisco Bay in the two-way coupled simulation, and in the far northwest in the one-way coupled simulation, are both associated with reduced 100-m wind speeds in Figure 10. These wind speed reductions may thus plausibly be consequences of the increased roughness.

To relate these roughness heights to changes in the wave state, we show significant wave heights (Figure 12). We see the passage of the front is accompanied by modestly increased wave heights (2 – 2.5 m), but the two-way coupled heights remain closer to the Morro Bay buoy measurements at 10 UTC (1.5 - 2.5 m) than in the one-way coupled simulation, before also increasing and becoming somewhat too high at 12 UTC. The higher roughness regions in both simulations are reflected by greater significant wave heights (2.5 - 3 m west of San Francisco in two-way; 4.5 - 5 m in the far northwest of one-way).

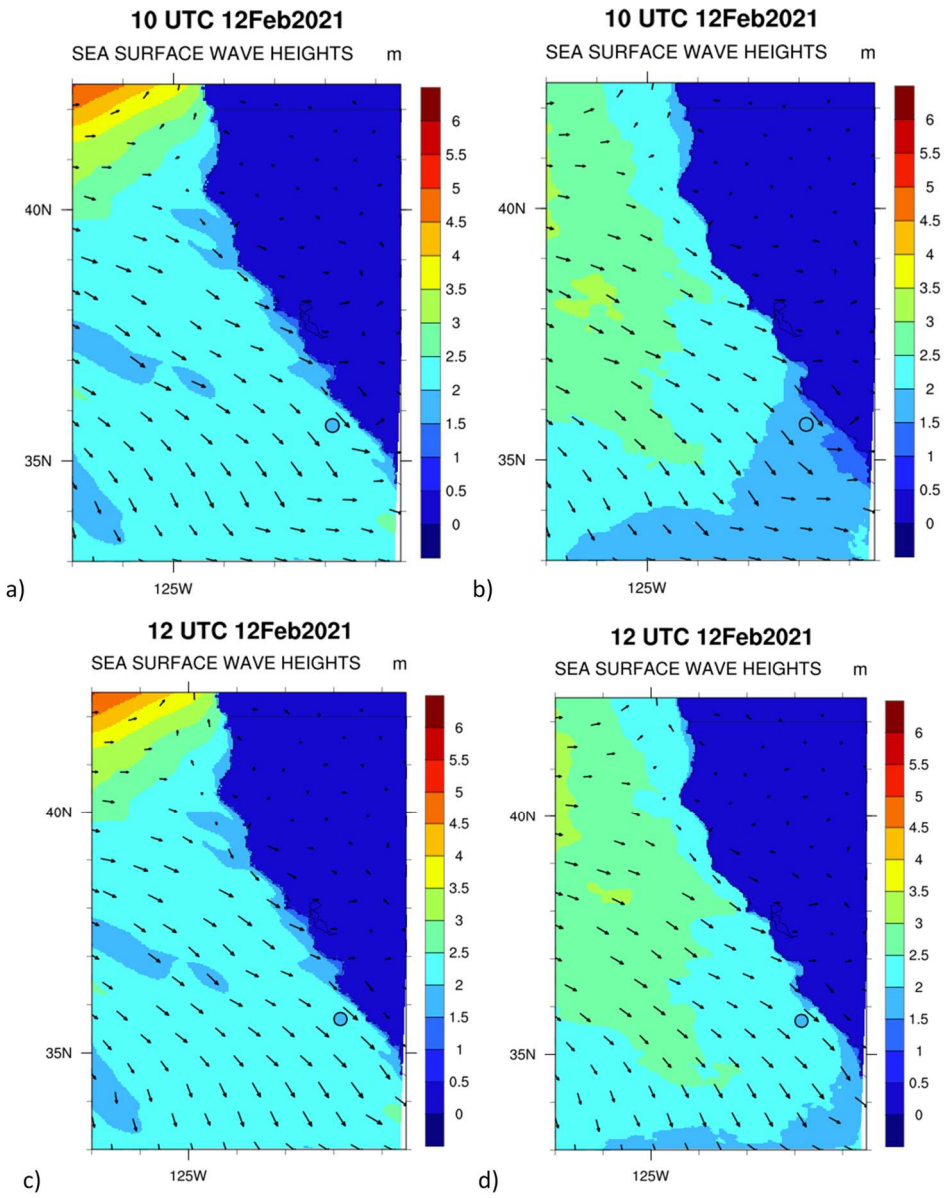

Figure 12. Simulated significant wave height in one-way coupled WRF (a, c), and two-way coupled WRF (b, d) simulations. Panels a-b are valid 10 UTC 12 Feb 2021; panels c-d are valid 12 UTC 12 Feb 2021. Location of and observed significant wave height at location of the Morro Bay lidar buoy is indicated by circle according to the same color scale.

A more extensive validation of WW3 fields at the location of the Morro Bay and Humboldt buoys, as well as at NDBC buoys 46028 (near Morro Bay) and 46022 (near Humboldt) is carried out by evaluating time series of significant wave height and peak wave period as shown in Figure 13. On these plots 'Baseline' is from the stand-alone WW3 simulation, 'WRF' is a separate stand-alone WW3 simulation driven by winds extracted from the stand-alone WRF simulation, and the dots represent observations when they are available. We see that for the two buoys near Morro Bay, WRF-driven WW3 clearly outperforms the Baseline WW3 run in terms of significant wave height after the frontal passage, correctly predicting a slower rate of increase and a reduced maximum value. While data from the Humboldt buoy are missing, the similar predictions at Buoy 46022 suggest that the WRF-driven run slightly better matches the observations after the frontal passage. Before the frontal passage both models are fairly close to the observed wave heights, and it is not clear either is superior.

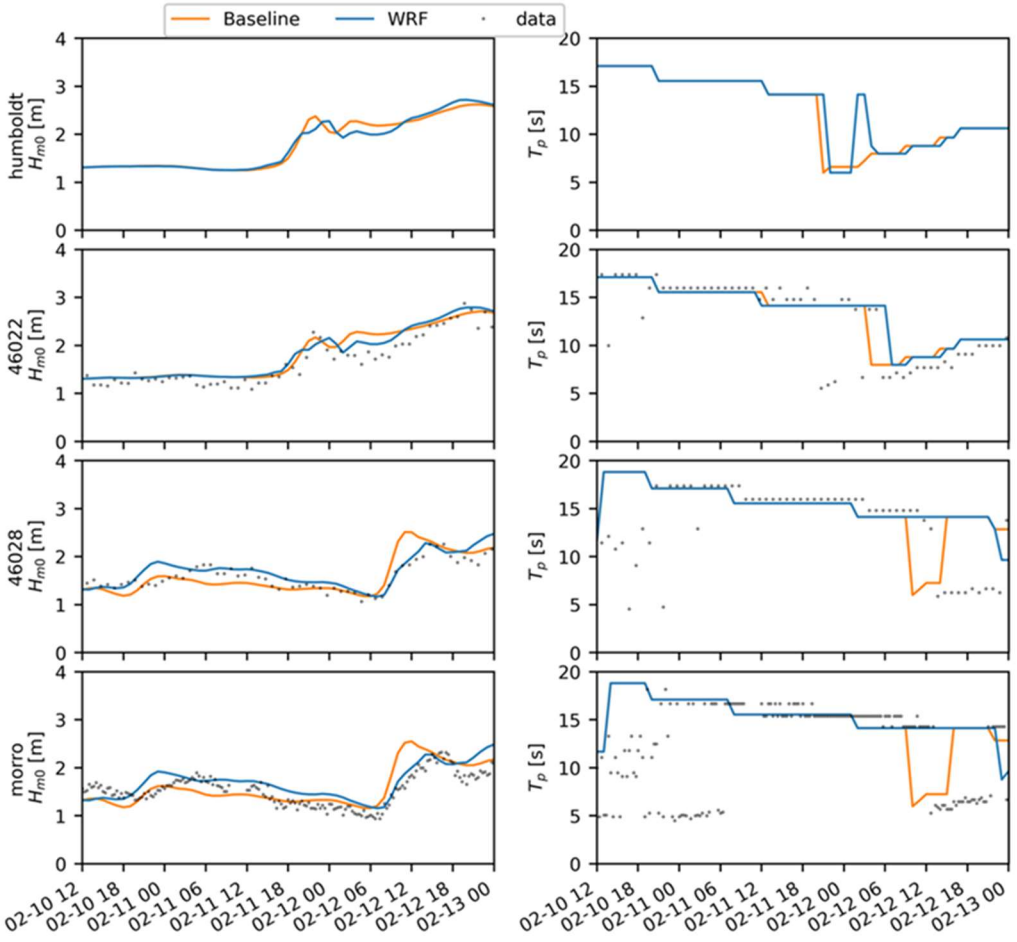

Figure 13. Time series of significant wave height (left column) and peak wave period (right column) at the location of the Humboldt and Morro Bay lidar buoys, and NDBC buoys 46022 (near Humboldt) and 46028 (near Morro Bay). Black dots indicate observations; orange curve is from Baseline WW3 simulation (driven by CFSv2 winds and used in the one-way coupled WRF simulation); blue curve is from WRF-driven WW3 simulation (driven by winds from the stand-alone WRF simulation).

When we examine the peak wave period, both observations and models tend to alternate between values of 15 seconds and greater, and values down around 5 seconds. This suggests that the wave spectra might be bimodal, with the longer period representing swell and the shorter period representing locally driven wind waves. This suggestion is confirmed in Figure 14, showing wave spectra at the four buoys at the 10 UTC and 12 UTC 12 Feb times. For the buoys near Morro Bay, both models reproduce the strongly bimodal spectra, but in the Baseline WW3 the higher frequency peak is about 0.14 Hz (i.e., period around 7 seconds) instead of the observed 0.2 Hz (period around 5 seconds), whereas the WRF-driven simulation has the location almost exact. The energy associated with this peak in the Baseline simulation also appears too large, accounting for the overestimation of significant wave height. For the buoys near Humboldt, the two models appear more similar, and neither can reproduce a bimodal spectrum as is apparent in the observations at Buoy 46022.

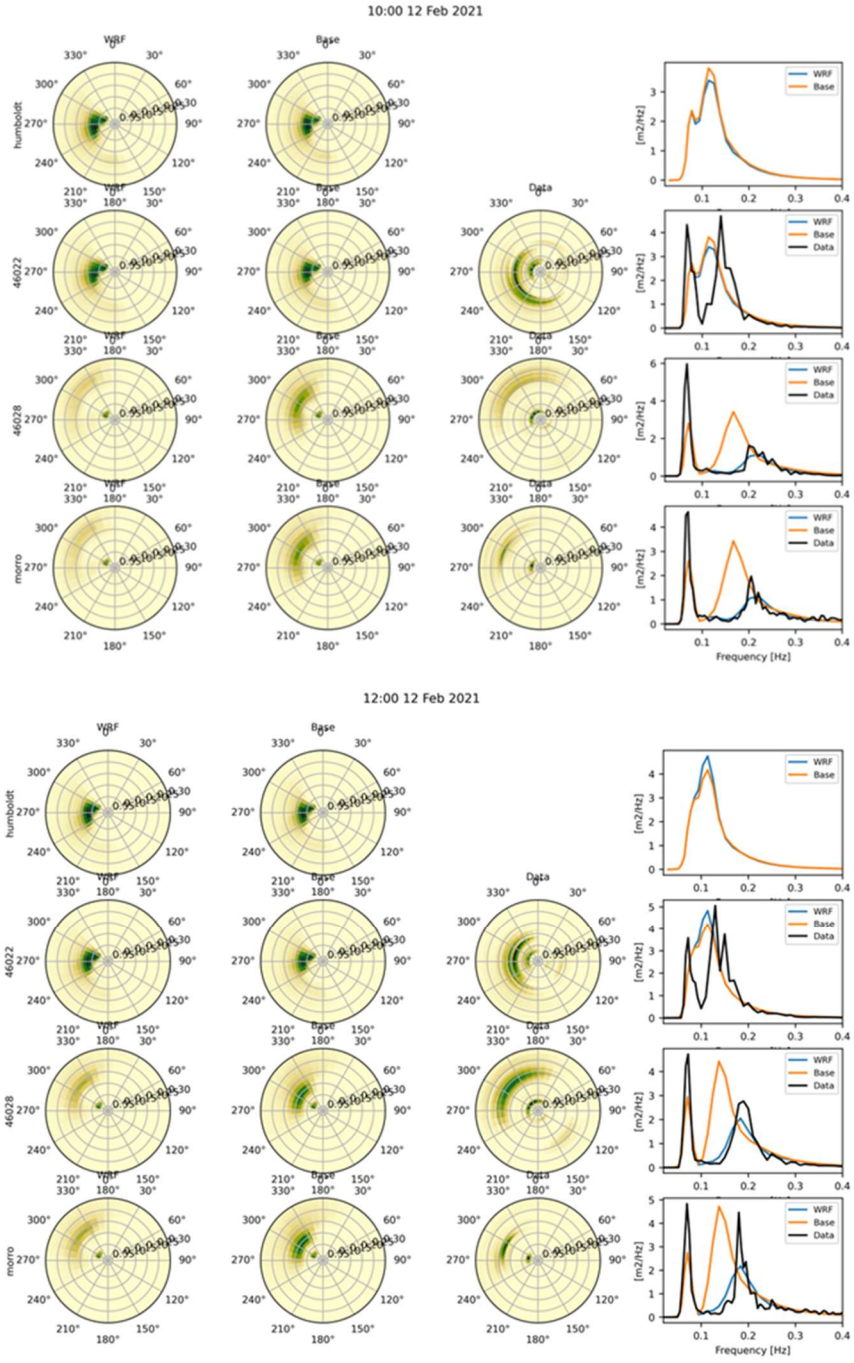

Figure 14. Directional and directionally averaged wave spectra at buoy locations in Figure... for 10 UTC 12 Feb (top) and 12 UTC 12 Feb (bottom). For directionally averaged spectra, color scheme is the same as in Figure 13. For the directional plots, left column is for WRF-driven WW3 simulation; middle column is for Baseline WW3 simulation; right column is from observations.

This case with two sharp but nearly equal spectral peaks, one of which is low-frequency swell, is a good example for which the use of the mean wavelength rather than the peak wavelength produces more representative results in the Taylor-Yelland parameterization. In deep water, a

wave with a period of 15 seconds has a wavelength of about 350 m, which when combined with a 2-meter significant wave height would give a Taylor-Yelland roughness of 0.2 microns (i.e., essentially laminar, for which a viscous correction would be used in practice). Furthermore, even if we assume the mean wavelength will mainly reflect the higher frequency mode, the overestimation of the period of this mode in the one-way coupled simulation by a factor of 1.4 will lead to overestimating the wavelength by a factor of two in deep water, which leads to a factor of nine difference in the Taylor-Yelland roughness height. This overestimation of period seems to account for the general low roughness values found throughout the central and southern CA coast in the one-way coupled simulation.

In summary, for this frontal passage case all model configurations seem to predict hub-height wind speeds at the Morro Bay buoy location fairly well, except all remain approximately one hour delayed with the initial wind ramp. To the extent that wave coupling changes the hub-height wind error, it makes it slightly worse by slightly increasing an already positive wind speed bias, which is consistent with somewhat smaller wave-based roughnesses than the stand-alone WRF COARE3.0-based roughness. However, the sensitivity to different roughness parameterization for this case is quite small, generally < 1 m s^{-1}.

Nevertheless, around and immediately after the frontal passage, there is clear evidence that wave fields in WW3 when driven by WRF are substantially closer to the observations, in the central and southern CA coast, including the Morro Bay area, than when driven by the CFSv2 reanalysis as in the one-way coupled WRF simulation. The improvement holds for both bulk quantities like significant wave height as well as the shape of the overall wave spectra. In particular, a more correctly placed wind-wave spectral peak in the two-way coupled simulation allows it to not have the pronounced underestimation of roughness height that the one-way coupled simulation exhibits around the time of frontal passage at Morro Bay. This shows the importance of using a two-way wind-wave coupled framework in conjunction with wave- and wave-roughness modeling off the CA coast.

5.2 Case of 10 Jul 2022

In early July 2022 there was a multi-day period of persistent northerly winds at the Humboldt buoy location. This pattern is consistent with the summer climatology of the region, during which the West Coast is under the influence of high pressure over the northern Pacific, leading to northerly synoptic winds, though for the period of interest, 10-13 Jul 2022, there was also surface high pressure over the Great Basin, inducing a thermal low in the Central Valley of California (Figure 15). Additionally, from 10-13 Jul 2022 these winds exhibited a diurnal cycle, being strongest around 12 UTC (predawn local time) and weakest around 00 UTC (late afternoon local time). Existing wind speed reanalysis products consistently underestimated the wind speed for this period, especially around the 12 UTC time frame, thus largely not capturing this nocturnal surge in wind speed (Figure 16).

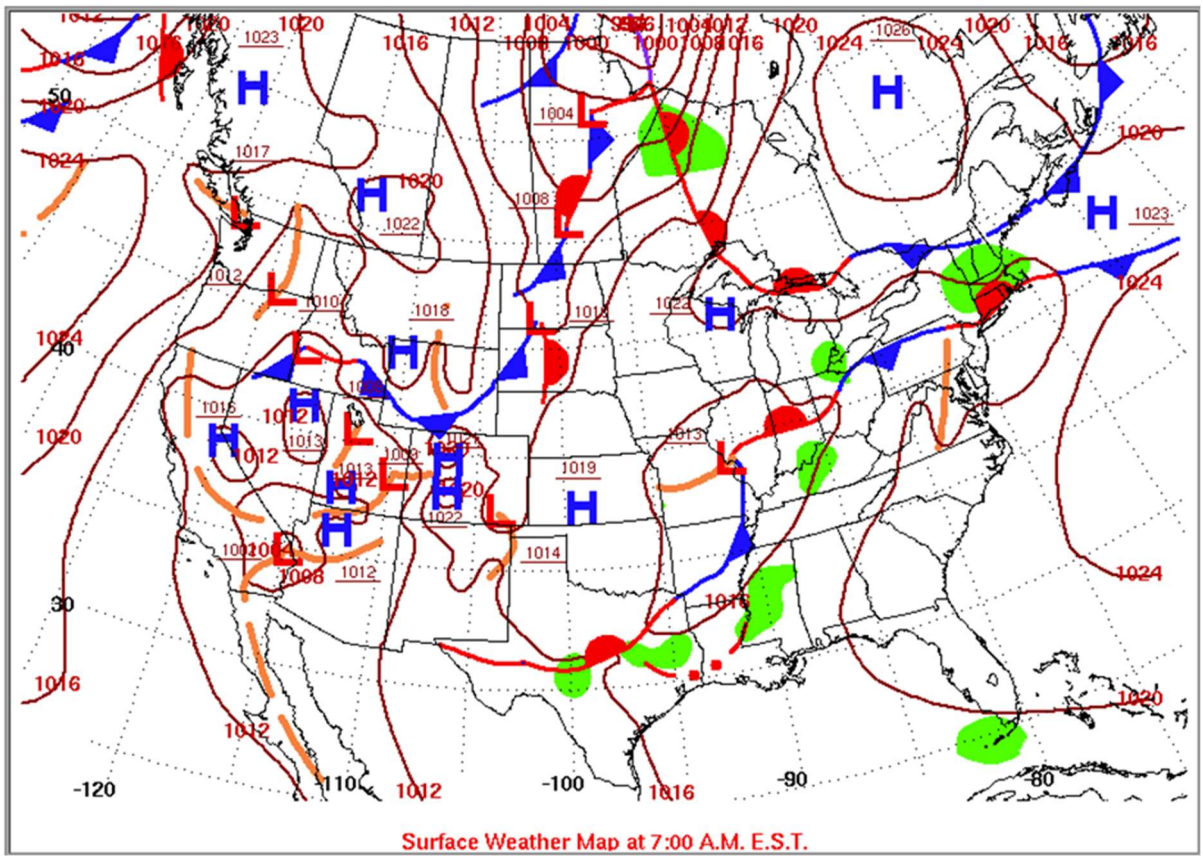

Figure 15. Synoptic weather maps for the morning of 12 Jul 2021. Courtesy National Centers for Environmental Prediction Weather Prediction Center.

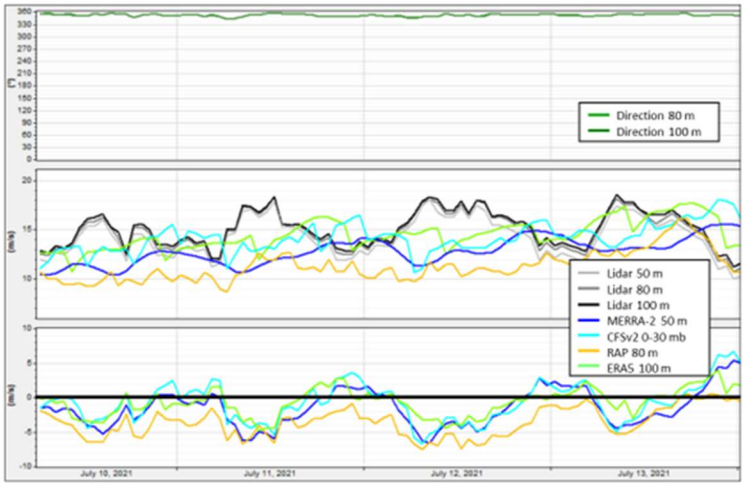

Figure 16. (Top) Time series of 100-m wind direction observed at the Humboldt lidar buoy. (Middle) Time series of 100-m wind speed at Humboldt location observed at lidar buoy (black) and for different reanalysis products (colored, labels given in figure). (Bottom) Time series of 100-m wind speed errors relative to Morro Bay lidar buoy.

The time series plot of lidar wind speeds vs. those in the WRF simulations are shown in Figure 17. It is apparent that the WRF simulations share the same general failure of the reanalysis

products to predict the nocturnal surges in wind speeds. The one-way wave-coupled simulation creates a fairly constant upward perturbation of about 2 m/s to the wind speed out to forecast hour 90, while the two-way coupled simulation has a consistent 1 m/s downward perturbation to the wind speed.

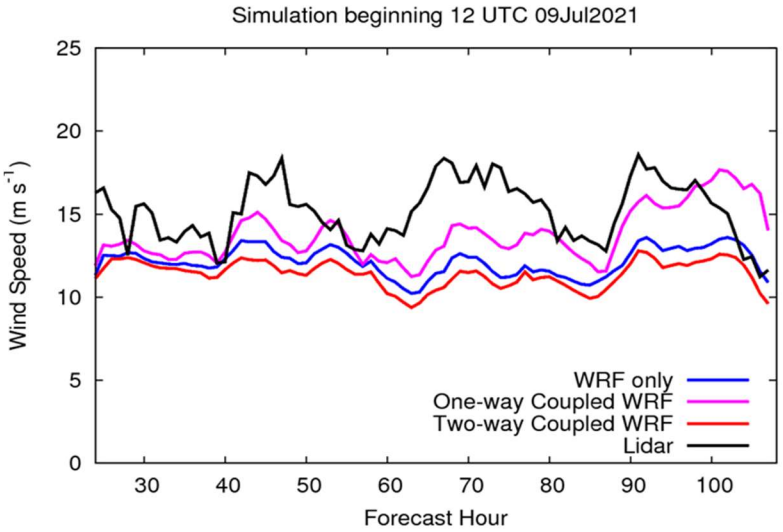

Figure 17. Time series of 100-m wind speed at Humboldt during 10 Jul 2021 case for lidar buoy (black), stand-alone WRF (blue), one-way coupled WRF (magenta) and two-way coupled WRF (red). Only period after forecast hour 24 (12 UTC 10 Jul 2021) is shown.

To gain more insight to this result, we examine a two-dimensional view of the baseline simulation (Figure 18a). The wind speeds clearly show many interesting patterns near the coast associated with irregularities of the coastline. A number of studies along the California coast (Winant et al. 1988; Söderberg and Tjernström 2001; Parish et al. 2016; Juliano et al. 2017) have shown that for the most part these are analogous to expansion fans / compression jumps forming downwind / upwind of capes, respectively.

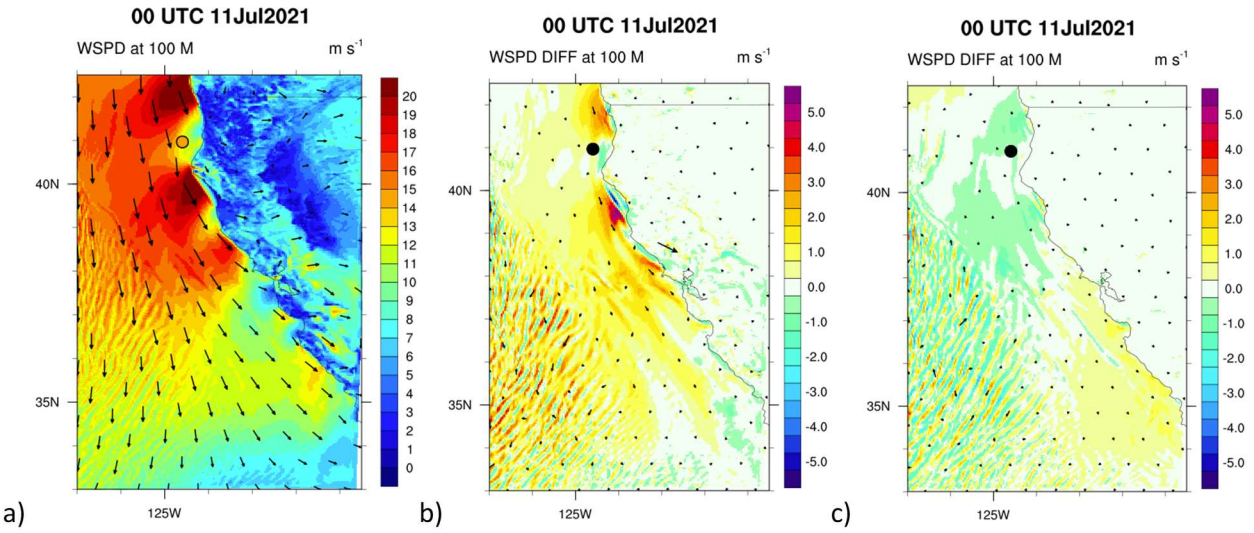

Figure 18. Simulated 100-m wind speed valid 00 UTC 11 Jul 2021 in stand-alone WRF simulation (a), and difference between simulated 100-m wind speed in one-way coupled (b) and two-way coupled (c) simulations from the stand-alone WRF simulation. For panel a, location of and observed 100-m wind speed at location of the Humboldt lidar buoy is indicated by circle according to the same color scale.

It can be noticed that these features extend approximately 50 km offshore, and that the Humboldt buoy is in an upstream blocking zone, not far from a strong gradient in wind speeds to its northwest. So while the winds speeds are clearly underestimated at the buoy location in the model, they are consistent with wind speeds at distances only a few model grid points away, thus indicating the importance of having resolution of at least a few km for these applications. However, it is also possible that the model wind speed error could also be due to errors in the vertical boundary layer structure, which we will explore in more detail later.

The one-way sensitivity plot (Figure 18b) shows that wind speeds are almost always increased relative to those in the baseline simulation, and the increases are generally greatest where the wind speeds themselves are greatest. By contrast, for the two-way simulation (Figure 18c) wind speeds are generally reduced west of a line through Point Arena, while they are increased to the east. This pattern does not seem to be associated with stability, because air / sea temperature differences have about the same (positive) value both east and west of this line along the coast. Rather, the two-way coupled winds seem to be reduced relative to the baseline when wind speeds are large, and increased when wind speeds are small. Thus, wave roughness in the two-way coupled simulation counteracts the wind speed variability relative to the baseline, the opposite of the tendency in the one-way coupled simulation.

A comparison of roughness heights in the simulations (Figure 19) shows that the trends of the one-way coupled simulation are predominantly due to the fact that the roughness values are nearly always much less than those of the baseline simulation regardless of wind speed. This increases the wind speeds in the one-way simulation relative to the baseline, and this increase is greatest for the cases where the baseline roughness is greatest, which for the baseline COARE parameterization is when baseline wind speed is greatest. Thus baseline wind speeds and one-way – baseline wind speeds are positively correlated. By contrast, the two-way coupled roughness values tend to be higher / lower when the baseline roughness / wind speeds are higher / lower, leading to the negative correlation between baseline wind speeds and two-way –

baseline wind speeds. But unlike for the one-way roughness, the two-way roughness spatial patterns are broadly consistent with those for the COARE parameterization.

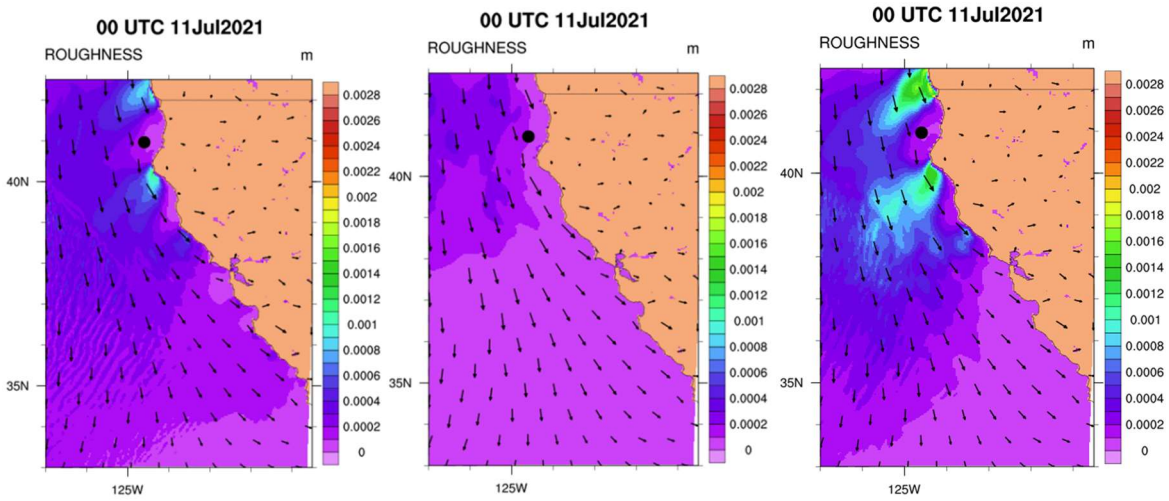

Figure 19. Simulated roughness height in stand-alone WRF simulation (a), one-way coupled WRF (b), and two-way coupled WRF (c) simulations, valid 00 UTC 11 Jul 2021. Location of Humboldt lidar buoy is indicated by circle.

When we look into the cause of these roughness differences in terms of wave fields, we find that the general reduced roughness in the one-way simulation is not necessarily due to smaller values of significant wave height. Figure 20 shows that offshore of northern California the one-way significant wave heights are larger than the two-way heights at this time, except within the expansion fans, which are not apparent at all in the one-way wave fields. The increased two-way roughness is primarily due to reduced values of mean wavelength than in the one-way simulation because the Taylor-Yelland roughness is a sharply increasing function of wave steepness. The likely reason for the one-way / two-way differences is that the two-way wave field is being driven by higher resolution wind fields and thus can better resolve smaller wavelength features. Furthermore, the two-way wind field can better capture the wind speed maxima / minima along the coastline, and the significant wave height is reflecting those spatial patterns.

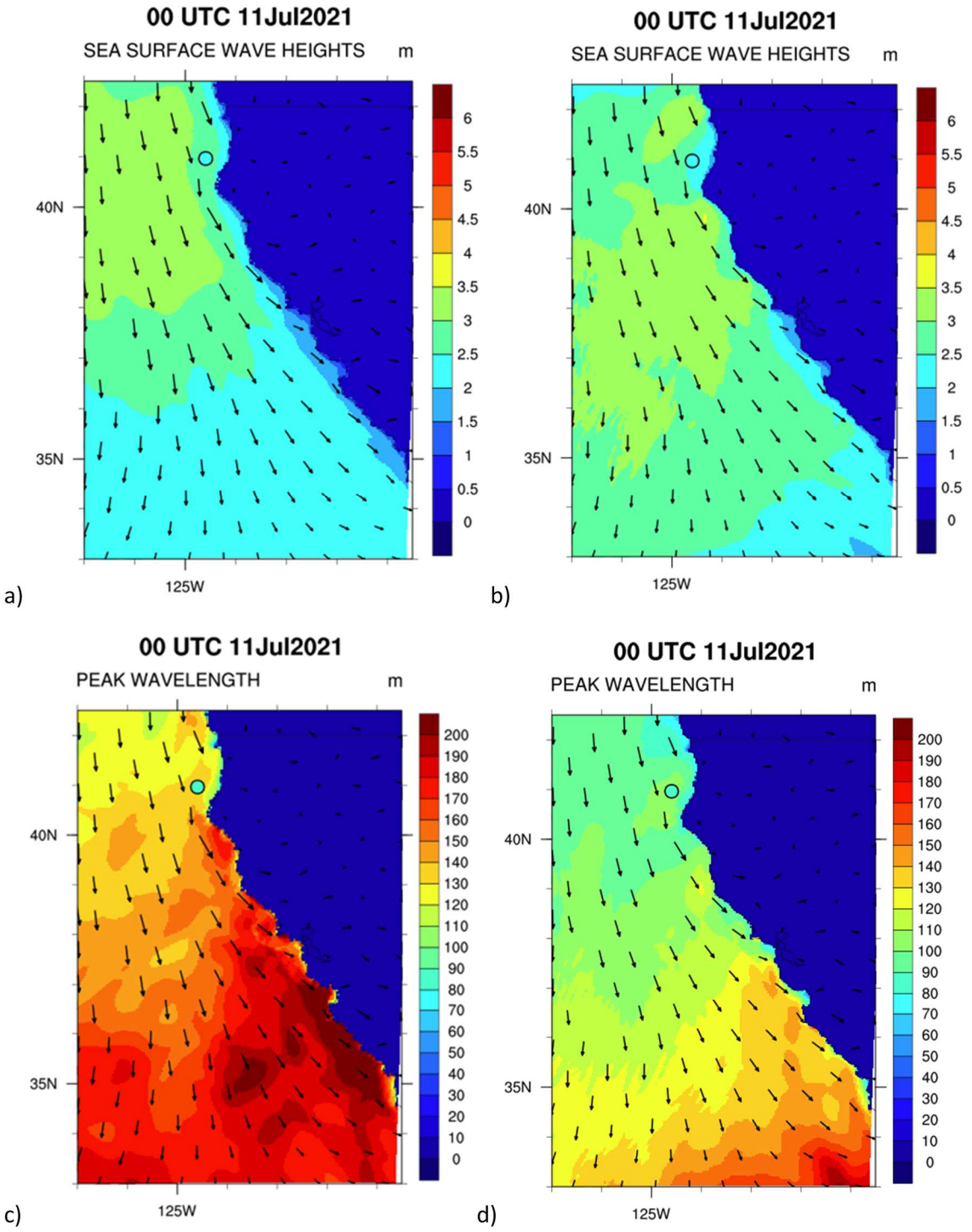

Figure 20. Simulated significant wave height (a, b) and mean wavelength (c, d) in one-way coupled WRF (a, c), and two-way coupled WRF (b, d) simulations, valid 00 UTC 11 Jul 2021. Location of and observed significant wave height at location of the Humboldt lidar buoy is indicated by circle according to the same color scale. Same is true of mean wavelength plots, except buoy value is shaded according to the observed peak wavelength.

At the location of the Humboldt buoy in Figure 20, the significant wave height is similar between the simulations, though it is somewhat smaller, and somewhat closer to the observations, in the two-way simulation. The two-way wave height field is more reflective of the wind speed maxima / minima patterns induced by the coastal topography than the one-way wave height field, which is what one would expect if the waves are responsive to the wind patterns, and these wind speed patterns are better resolved in the two-way simulation. Though the one-way and two-way significant wave heights are comparable, the mean wavelength of the two-way simulation is substantially closer to the observed peak wavelength than the one-way, though still somewhat too high. While the one-way simulation bulk wave parameters have larger errors relative to the Humboldt buoy than those for the two-way, but the errors partially self-cancel in the roughness length computation, leading to the relative similarity at the buoy between Figures 20b and c. Note that the mean wavelength is generally less than the peak wavelength, so the model overestimation of wavelength relative to the buoy should hold regardless of which is used.

A time series comparison of wave fields between the stand-alone WW3 simulation and the WRF-driven WW3 simulation, is shown in Figure 21, this time showing other buoy locations. It is apparent that for the northern buoys the WRF-driven wave heights match the observations much better than the stand-alone wave heights, which tend to be too high. There is a diurnal cycle to the wave heights in the stand-alone (Baseline) WW3 simulation for the Humboldt Buoy and Buoy 4602, but it is out of phase relative to the observed diurnal cycle (i.e., peaking a little before 00 UTC vs. a little before 12 UTC in the observations) , whereas the main error for the WRF-driven wave heights is the absence of a diurnal cycle. The peak wave period of stand-alone WW3 is also sometimes, though not always, higher than for the buoy and WRF-driven WW3. Thus the previous results seem fairly robust, at least for northern CA.

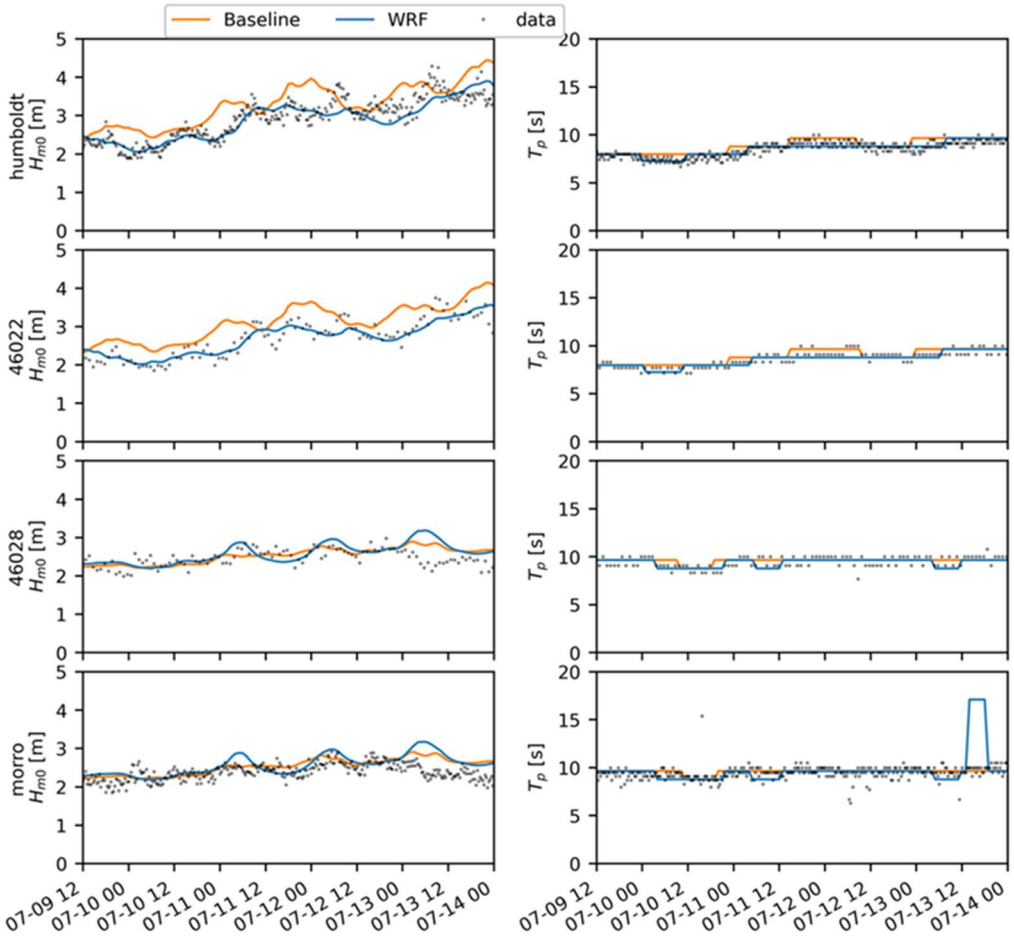

Figure 21. Time series of significant wave height (left column) and peak wave period (right column) at the location of the Humboldt and Morro Bay lidar buoys, and NDBC buoys 46022 (near Humboldt) and 46028 (near Morro Bay). Black dots indicate observations; orange curve is from Baseline WW3 simulation (driven by CFSv2 winds and used in the one-way coupled WRF simulation); blue curve is from WRF-driven WW3 simulation (driven by winds from the stand-alone WRF simulation).

From the above analysis we conclude that the two-way coupled wave fields are reasonably close to observations around the Humboldt buoy, superior to those from the one-way coupled simulation, and lead to parameterized roughness that is physically plausible and consistent with the COARE parameterizations. This leads us back to the question of the model underestimation of wind speeds, especially during the nocturnal surges. We conclude that processes other than wave roughness are accounting for the differences of wind speed from the observations.

We believe that the differences are closely related to the inability of the model to capture the detailed heat and radiative fluxes associated with cloudy marine boundary layers.

Daily satellite imagery from this period (Figure 22) clearly shows extensive low-level coastal cloudiness except in the expansion fan areas. While cloud cover is not directly measured by the buoy, pyranometer solar flux data from the buoy shows the potential maximum value for this

period is not achieved on most of the days (Figure 23). While the model reproduces this cloud field to some extent, it is mostly away from the buoy location, at least during the daytime hours.

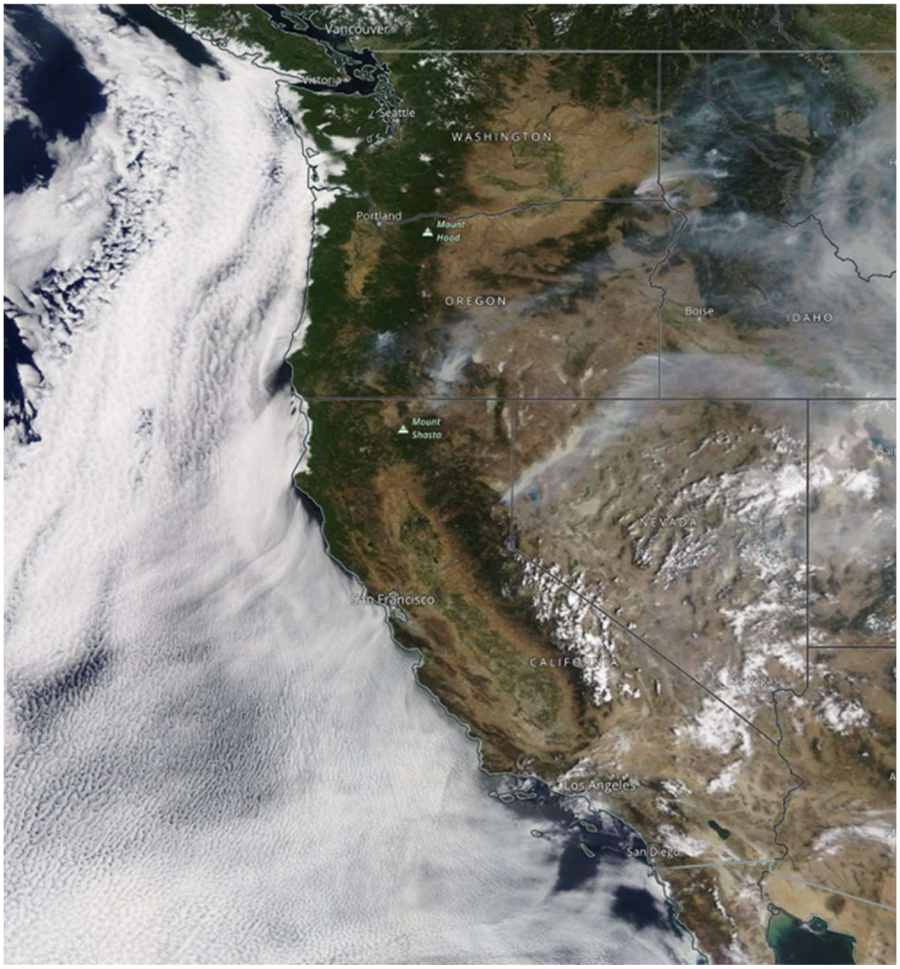

Figure 22. Visible reflectance of U.S. Pacific Coast from Terra / MODIS on 10 Jul 2021. Courtesy NASA Worldview.

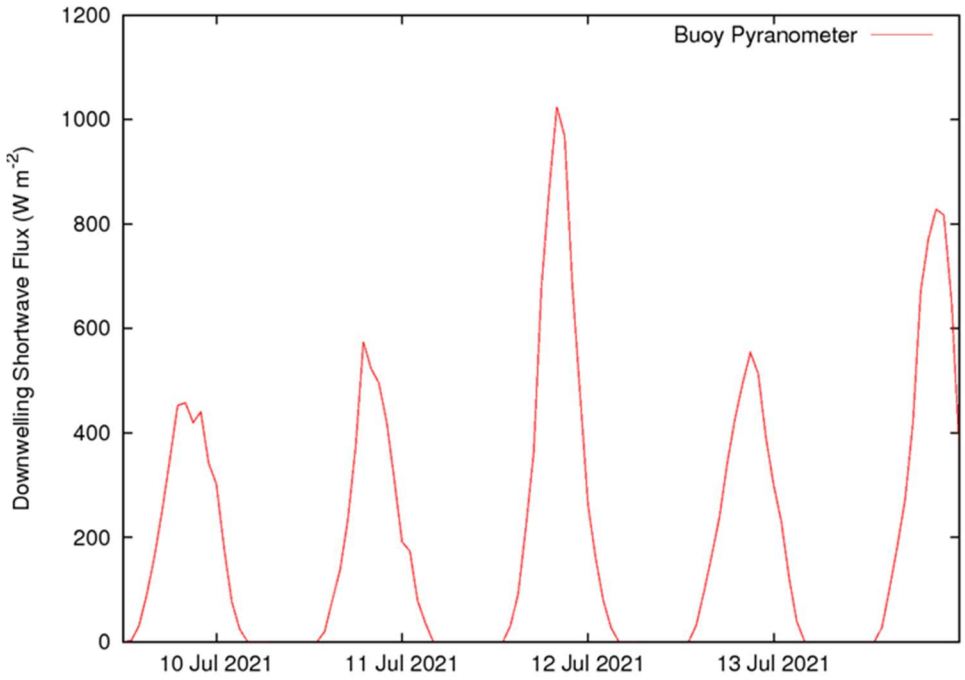

Figure 23. Time series of downwelling shortwave flux as measured by pyranometer on Humboldt lidar buoy.

For nighttime cloudiness, which corresponds to the time period of the wind surges, some information can be gleaned by using the buoy temperature and relative humidity measurements to compute the spread between temperature (T) and dewpoint (Td). The lifting condensation level, a proxy for cloud base height, is to first approximation directly proportional to this spread. What we find (Figure 24) is: 1) Buoy T and T_d show a strong diurnal trend; model T and especially T_d do not. 2) While buoy T and T_d tend to be highly correlated, their spread and hence lifting condensation level also has a diurnal cycle, being larger in daytime than in nighttime. This is consistent with the behavior of marine stratocumulus, which tend to be driven by cloud top radiative cooling and are suppressed by solar heating in daytime, but the model spread does not have this diurnal trend and is smaller in magnitude. 3) At night buoy T_d tends to be well below buoy SST, while model T_d more or less tracks model SST.

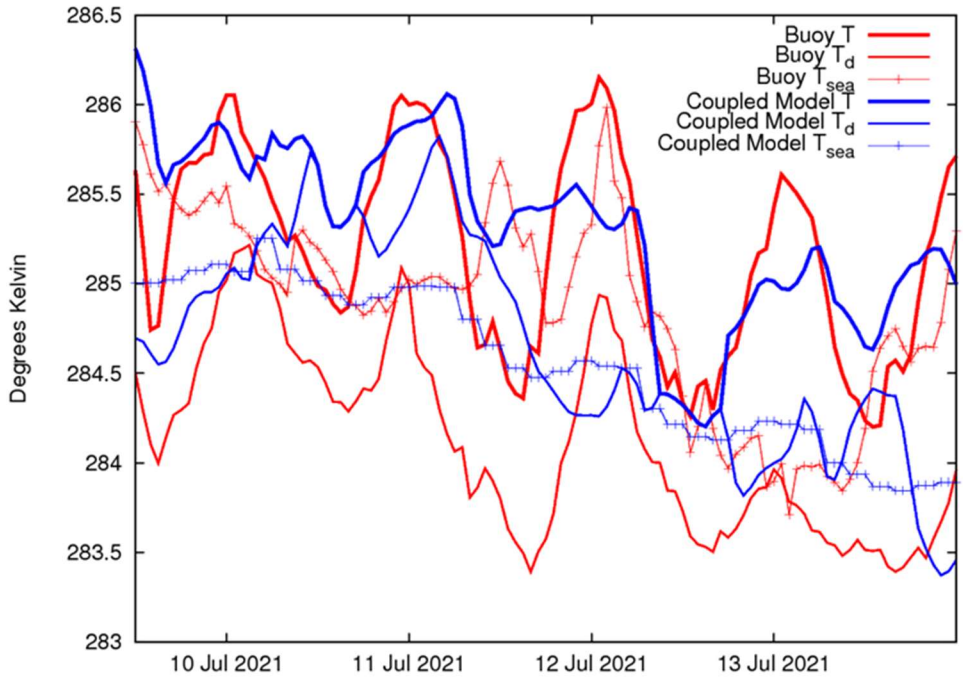

Figure 24. Time series of near-surface air temperature, near-surface dewpoint temperature, and sea surface temperature at location of Humboldt buoy from observations (red) and two-way coupled model simulation (blue).

We note that Liu et al. (2024) had performed a more extensive series of simulations in the region, and had used the lidar buoy data to conclude that use of the MYNN boundary layer parameterization led to significant positive wind speed bias in generally northerly flow conditions which were alleviated when using YSU. The positive bias was associated with warm coastal air temperatures, which tend to increase the air temperature – sea temperature metric of stability, while the YSU scheme did not have as much of a temperature bias. The current results do not contradict this overall tendency, and the mean temperature trends of the model track the buoy observations reasonably well, but it does suggest that processes on smaller spatial and temporal scale like radiation and cloud microphysics can at times play a significant role in hub-height wind speed biases.

In summary, we conclude that the nocturnal wind surges for this period reflect enhanced downward mixing of momentum in the cloudy marine boundary layers, but that this process is not being properly represented in the models. Further investigation of this is beyond the scope of this work. However, we can also see evidence that wave-based roughness from a two-way coupled simulation helps eliminate systematic wind speeds biases from a one-way coupled framework that can be on the order of 10%, and better captures mesoscale flow features.

6.0 Conclusions

The DOE lidar buoy deployment off the U.S. Pacific Coast provided a unique opportunity for long-term validation of its hub-height wind resource, in conjunction with a suite of meteorological, oceanographic, and radiometric measurements. In this study we show results from performing atmosphere / wave-coupled simulations over the locations of the U.S. West Coast lidar buoy deployment for cases where hub-height wind speed was not well simulated by existing reanalysis products. The methodology, similar to that of the East Coast Gaudet et al. (2022) study, involved comparing wind fields from stand-alone, one-way wave-coupled, and two-way wave-coupled WRF atmospheric simulations, as well as fields in the wave model (WW3) when driven by the stand-alone atmospheric model. Both wind and wave fields were validated against data from the lidar buoys, as well as neighboring buoys maintained by the NDBC.

We found that including the effect of wave coupling did not improve model error for the cases considered here (as well as for other cases examined but not shown here). For the Feb 2021 Morro Bay frontal passage case, the main source of model error at the Morro Bay buoy was a timing error of the wind ramp associated with the frontal passage; this remained for our in-house WRF-driven models. Apart from the timing error, all of the in-house model wind speed errors were small, regardless of coupling method, which had little impact on this metric. For the Jul 2021 Humboldt low-level jet case, the strong negative nocturnal wind speed biases in the reanalysis products persisted in the WRF simulations at the Humboldt buoy, and in fact were somewhat worse in the two-way coupled simulations.

We conclude that at least for these two cases the model wind speed errors at the buoy were due to factors other than the representation of wind-wave coupling. For the Feb 2021 case the cause of the model timing error is unknown but it seems to be present in virtually all model products and wave coupling variants. For the Jul 2021 case we make a plausible argument that model representation of the diurnal evolution of the marine boundary layer, and its associated cloudiness, is the main source of model error.

These findings notwithstanding, a more holistic analysis of the simulations in these cases yielded the following results:

- For the warm season coastal jet case in particular, very large horizontal gradients in wind speed features were apparent in the models a few kilometers from the Humboldt buoy, due to the impact of the coastal capes and topography on the flow. This is consistent with a finding from the East Coast study that kilometer-scale resolution, or finer, is needed to minimize model error for these near-coast applications.
- For the cases studied (one cold season, one warm season), the use of wave-based roughness parameterization can have a 1-2 m s^{-1} impact on winds at hub height (~ 100 m). Consistent with results seen on the East Coast, the sensitivity might be somewhat higher during the stable warm season case than the more unstable cold season case.
- In both cases observed wave bulk and spectral properties were better predicted when driven by winds from the WRF model configuration than from a global reanalysis, showing the value of running a two-way WRF-WW3 coupled configuration over a one-way coupled WRF-WW3 configuration using a stand-alone WW3 simulation.
- In particular, the one-way coupled simulation was prone to producing large regions of minimal wave roughness relative to the COARE parameterization and overpredicted wind

speed, primarily due to overpredicting the characteristic wavelength and periods of the wave field. This is in contrast to the East Coast study, where one-way coupling also produced a systematic bias in the wind speed, but where the bias was underprediction of wind speed.

- The two-way coupled simulation tended to show less systematic bias in roughness relative to the COARE wind speed parameterizations and could be either positive or negative in the model domain, consistent with the East Coast study.
- The use of the mean wavelength instead of the peak wavelength in the Taylor-Yelland roughness parameterization did help to mitigate against severe underprediction of roughness in the presence of swell relative to the COARE parameterization but did not completely eliminate it.

These results suggest that at least a kilometer-scale wind field, and two-way wind-wave coupling, are needed to provide the best representation of hub-height wind / wave coupling, as well as the importance of combining observational profiles derived from lidar buoys with a sufficiently dense network of other sensors to validate these models.

However, sufficient resolution will not of itself necessarily lead to reduced model wind speed errors without the proper representation of all the physics of the marine boundary layer. We note that Liu et al. (2024) had compared simulations with the YSU PBL parameterization with those using the MYNN PBL parameterization over the Humboldt region in Jul 2021. They found that generally the MYNN simulation had larger positive wind speed biases, which they attributed to insufficient cloud cover in the MYNN increasing the coastal land downwelling shortwave radiation and temperatures, which enhance the land/sea thermal contrast and increase wind speed by the thermal wind relation. For our shorter-term simulations, which use the YSU parameterization, we similarly implicate insufficient cloud coverage and its radiative impact, but we focus on nocturnal negative wind speed biases and their apparent relation to the longwave radiation budget. Clearly improved model representation of all these effects are needed.

Future studies in the region should also include coupling to an oceanic model in addition to wind / wave coupling. In particular, the frequent strong along-shore jets lead to near-shore upwelling of cold subsurface waters, which in turn can have significant impacts on winds and atmospheric boundary layer structure. The COAWST framework includes the capability of adding two-way coupling with the Regional Oceanic Modeling System to WRF / WW3 coupling, but this capability was not used in this study.

As in the East Coast study of Gaudet et al. (2022), using a one-way atmospheric / wave coupling system tended to introduce systematic wind speed biases that were alleviated in the two-way coupled system, primarily due to the improved representation of the wind field. Unlike that study, however, those systematic biases tended to be positive instead of negative. It is likely this is due to the deep water environment off the U.S. West Coast vs. the shallow environment off the U.S. East Coast, which leads to increased characteristic wavelengths and reduced steepness and roughness in the Taylor and Yelland parameterization. So these results suggest that different parameterizations of wave roughness as a function of bulk wave fields might be needed for each region. While modifying the Taylor-Yelland roughness parameterization did seem to help prevent large biases in the two-way coupled simulation in the presence of swell, improved methods for predicting deep-water swell-driven roughness are still needed, such as the Porchetta et al. (2019) scheme that accounts for wind / wave misalignment.

7.0 References

Amante, C., and B. W. Eakins. 2009. “ETOPO1 1 Arc-Minute Global Relief Model: Procedures, Data Sources and Analysis.” NOAA Technical Memorandum NESDIS NGDC-24.

Ardhuin, F., E. Rogers, A.V. Babanin, J.-F. Filipot, R. Magne, A. Roland, A. van der Westhuysen, et al., 2010: Semiempirical dissipation source functions for ocean waves. Part I: Definition, calibration, and validation. Journal of Physical Oceanography 40(9), 1917–41, https://doi.org/10.1175/2010JPO4324.1.

Battjes, J. A., and J.P.F.M. Janssen, 1978: Energy loss and set-up due to breaking of random waves. 16th International Conference on Coastal Engineering, 569–87. Hamburg, Germany, ASCE.

Benjamin, S. G., S.S. Weygandt, J.M. Brown, M. Hu, C.R. Alexander, T.G. Smirnova, J.B. Olson, E.P. James, D.C. Dowell, G.A. Grell, H. Lin, S.E. Peckham, T.L. Smith, W.R. Moninger, J.S. Kenyon, and G.S. Manikin, 2016: A North American hourly assimilation and model forecast cycle: The Rapid Refresh. Monthly Weather Review, 144(4), 1669-1694, https://doi.org/10.1175/MWR-D-15-0242.1.

Drennan, W. M., P.K. Taylor, and M.J. Yelland, 2005: Parameterizing the sea surface roughness. Journal of Physical Oceanography, 35(5), 835-848, https://doi.org/10.1175/JPO2704.1.

Edson, J. B., and C.W. Fairall, 1998: Similarity relationships in the marine atmospheric surface layer for terms in the TKE and scalar variance budgets. Journal of the Atmospheric Sciences, 55(13), 2311-2328, https://doi.org/10.1175/1520-0469(1998)055<2311:SRITMA>2.0.CO;2.

Edson, J. B., V. Jampana, R.A. Weller, S.P. Bigorre, A.J. Plueddemann, C.W. Fairall, S.D. Miller, L. Mahrt, D. Vickers, and H. Hersbach, 2013: On the exchange of momentum over the open ocean. Journal of Physical Oceanography, 43(8), 1589-1610, https://doi.org/10.1175/JPO-D-12-0173.1.

Ellenson, A., and H. T. Özkan-Haller, 2018: Predicting large ocean wave events characterized by bimodal energy spectra in the presence of a low-level southerly wind feature. Wea. Forecasting, 33 (2), 479–99. https://doi.org/10.1175/WAF-D-17-0035.1

Fairall C.W., E.F. Bradley, J.E. Hare, A.A. Grachev, and J.B. Edson, 2003: Bulk parameterization of air–sea fluxes: Updates and verification for the COARE algorithm. Journal of Climate, 16, 571-591, https://doi.org/10.1175/1520-0442(2003)016<0571:BPOASF>2.0.CO;2.

García Medina, G., W.J. Shaw, Z. Yang, and R.K. Newsom, 2020: “Mid-Atlantic Bight Wave Hindcast To Support DOE Lidar Buoy Deployments: Model Validation.” https://doi.org/10.2172/1635751.

Gaudet, B.J., G. García Medina, R. Krishnamurthy, W.J. Shaw, L.M. Sheridan, Z. Yang, R.K. Newsom, and M. Pekour, 2022: Evaluation of coupled wind / wave model simulations of offshore winds in the Mid-Atlantic Bight using lidar-equipped buoys. Mon. Wea. Rev., 150, 1377–1395, https://doi.org/10.1175/MWR-D-21-0166.1.

Gelaro, R., W. McCarty, M.J. Suárez, et al., 2017: The Modern-Era Retrospective Analysis for Research and Applications, Version 2 (MERRA-2). Journal of Climate, 30, 5419-5454, https://doi.org/10.1175/JCLI-D-16-0758.1.

Golbazi, M., and C.L. Archer, 2019. Methods to estimate surface roughness length for offshore wind energy. Adv Meteorol. 2019:5695481. https://doi.org/10.1155/2019/5695481

Hasselmann, K., T.P. Barnett, E. Bouws, H. Carlson, D.E. Cartwright, K. Enke, J.A. Ewing, et al., 1973: Measurements of wind-wave growth and swell decay during the Joint North Sea Wave Project (JONSWAP). Ergaenzungsheft Zur Deutschen Hydrographischen Zeitschrift A, 12: 95 pp.

Hasselmann, S., K. Hasselmann, J.H. Allender, and T.P. Barnett, 1985: Computations and parameterizations of the nonlinear energy transfer in a gravity-wave spectrum. Part II: Parameterizations of the nonlinear energy transfer for application in wave models. Journal of Physical Oceanography, 15, 1378–91, https://doi.org/10.1175/1520-0485(1985)015<1378:CAPOTN>2.0.CO;2.

Hersbach, H., B. Bell, P. Berrisford, et al., 2020: The ERA5 global reanalysis. Quarterly Journal of the Royal Meteorological Society, 146, 1999– 2049, https://doi.org/10.1002/qj.3803.

Hong, S.-Y., Y. Noh, and J. Dudhia, 2006: A new vertical diffusion package with an explicit treatment of entrainment processes. Mon. Wea. Rev., 134, 2318–2341, https://doi.org/10.1175/MWR3199.1.

Jiménez, P. A., and J. Dudhia, 2018: On the need to modify the sea surface roughness formulation over shallow waters. Journal of Applied Meteorology and Climatology, 57, 1101-1110, https://doi.org/10.1175/JAMC-D-17-0137.1.

Jones, P.W., 1998: A Users Guide for SCRIP: A Spherical Coordinate Remapping and Interpolation Package. V 1.4, Los Alamos National Laboratory.

Juliano, T. W., T. R. Parish, D. A. Rahn, and D. C. Leon, 2017: An Atmospheric Hydraulic Jump in the Santa Barbara Channel. J. Appl. Meteor. Climatol., 56, 2981–2998, https://doi.org/10.1175/JAMC-D-16-0396.1.

Krishnamurthy R., G. Garcia Medina, B.J. Gaudet, W.I. Gustafson, E.I. Kassianov, J. Liu, and R.K. Newsom, et al. 2023. "Year-long Buoy-Based Observations of the Air-Sea Transition Zone off the U.S. West Coast." Earth System Science Data 15, no. 12:5667–5699. https://doi.org/10.5194/essd-15-5667-2023.

Liu Y., B.J. Gaudet, R. Krishnamurthy, S. Tai, L.K. Berg, N. Bodini, and A. Rybchuk, et al. 2024. "Identifying meteorological drivers for errors in modeled winds along the Northern California Coast." Monthly Weather Review 152, no. 2:455–469. https://doi.org/10.1175/MWR-D-23-0030.1.

Mentaschi, L., G. Besio, F. Cassola, and A. Mazzino, A., 2015: Performance evaluation of Wavewatch III in the Mediterranean Sea. Ocean Modelling, 90, 82–94, https://doi.org/10.1016/j.ocemod.2015.04.003.

Musial, W., Spitsen, P., Beiter, P., Duffy, P., Marquis, M., Cooperman, A., Hammond, R., and Shields, M.: 2021. Offshore Wind Market Report: 2021 Edition, DOE/GO-102021-5614, National Renewable Energy Laboratory (NREL), Golden, CO (United States), https://doi.org/10.2172/1818842.

Nakanishi, M., and H. Niino, 2009: Development of an improved turbulence closure model for the atmospheric boundary layer. J. Meteor. Soc. Japan, 87, 895–912, https://doi.org/10.2151/jmsj.87.895.

Newsom, R. K., 2016: Optimizing Lidar Wind Measurements from the DOE WindSentinel Buoys. (No. PNNL-25512). Pacific Northwest National Lab. (PNNL), Richland, WA (United States).

Oost, W., G. Komen, C. Jacobs, et al., 2002: New evidence for a relation between wind stress and wave age from measurements during ASGAMAGE. Boundary-Layer Meteorology, 103, 409–438, https://doi.org/10.1023/A:1014913624535.

Parish, T. R., D. A. Rahn, and D. C. Leon, 2016: Aircraft Measurements and Numerical Simulations of an Expansion Fan off the California Coast. J. Appl. Meteor. Climatol., 55, 2053–2062, https://doi.org/10.1175/JAMC-D-16-0101.1.

Pérez, J., M. Menendez, and I.J. Losada, 2017: GOW2: A global wave hindcast for coastal applications. Coastal Engineering, 124, 1–11., https://doi.org/10.1016/j.coastaleng.2017.03.005.

Pérez, J., F. J. Méndez, M. Menéndez, and I. J. Losada, 2014. ESTELA: A method for evaluating the source and travel time of the wave energy reaching a local area. Ocean Dynamics, 64 (8), 1181–91. https://doi.org/10.1007/s10236-014-0740-7.

Porchetta, S., Temel, O., Muñoz-Esparza, D., Reuder, J., Monbaliu, J., van Beeck, J., and van Lipzig, N., 2019: A new roughness length parameterization accounting for wind–wave (mis)alignment, Atmos. Chem. Phys., 19, 6681–6700, https://doi.org/10.5194/acp-19-6681-2019.

Rascle, N., and F. Ardhuin, 2013: A global wave parameter database for geophysical applications. Part 2: Model validation with improved source term parameterization. Ocean Modelling, 70, 174–188, https://doi.org/10.1016/j.ocemod.2012.12.001.

Saha, S., S. Moorthi, H.-L. Pan, et al., 2010: The NCEP Climate Forecast System Reanalysis. Bulletin of the American Meteorological Society, 91, 1015-1057, https://doi.org/10.1175/2010BAMS3001.1.

Saha, S., S. Moorthi, X. Wu, J. Wang, S. Nadiga, P. Tripp, D. Behringer, et al., 2014: The NCEP Climate Forecast System Version 2. Journal of Climate, 27 (6), 2185–2208, https://doi.org/10.1175/JCLI-D-12-00823.1.

Sauvage, C., Seo, H., Clayson, C. A., & Edson, J. B. (2023). Improving wave-based air-sea momentum flux parameterization in mixed seas. Journal of Geophysical Research: Oceans, 128, e2022JC019277. https://doi.org/10.1029/2022JC019277.

Shaw, W. J., J. Draher, G. Garcia Medina, A.M. Gorton, R. Krishnamurthy, R.K. Newsom, et al., 2020: General Analysis of Data Collected from DOE Lidar Buoy Deployments Off Virginia and New Jersey (No. PNNL-29823). Pacific Northwest National Lab. (PNNL), Richland, WA (United States).

Sheridan, L. M., R. Krishnamurthy, A.M. Gorton, W.J. Shaw, and R.K. Newsom, 2020: Validation of reanalysis-based offshore wind resource characterization using lidar buoy observations. Marine Technology Society Journal, 54(6), 44-61, https://doi.org/10.4031/MTSJ.54.6.13.

Sheridan, L. M., R. Krishnamurthy, and B.J. Gaudet, 2021: Assessment of Model Hub Height Wind Speed Performance Using DOE Lidar Buoy Data (No. PNNL-30840). Pacific Northwest National Laboratory (PNNL), Richland, WA (United States).

Sheridan, L. M., Krishnamurthy, R., García Medina, G., Gaudet, B. J., Gustafson Jr., W. I., Mahon, A. M., Shaw, W. J., Newsom, R. K., Pekour, M., and Yang, Z., 2022: Offshore reanalysis wind speed assessment across the wind turbine rotor layer off the United States Pacific coast, Wind Energ. Sci., 7, 2059–2084, https://doi.org/10.5194/wes-7-2059-2022.

Skamarock, W. C., J.B. Klemp, J. Dudhia, D.O. Gill, Z. Liu, J. Berner, et al., 2019: A Description of the Advanced Research WRF Model Version 4 (No. NCAR/TN-556+STR), https://doi.org/10.5065/1dfh-6p97.

Smith, S. D., and Coauthors, 1992: Sea surface wind stress and drag coefficients: The HEXOS results. Bound.-Layer Meteor., 60, 109–142.

Söderberg, S., and M. Tjernström, 2001: Supercritical channel flow in the coastal atmospheric boundary layer: Idealized numerical simulations. J. Geophys. Res., 106, 17811–17829.

Stopa, J. E., 2018: Wind forcing calibration and wave hindcast comparison using multiple reanalysis and merged satellite wind datasets. Ocean Modelling, 127, J55–69. https://doi.org/10.1016/j.ocemod.2018.04.008.

Taylor, P.K., and M.A. Yelland, 2001: The dependence of sea surface roughness on the height and steepness of the waves. Journal of Physical Oceanography, 31, 572-590, https://doi.org/10.1175/1520-0485(2001)031<0572:TDOSSR>2.0.CO;2

Warner, J.C., B. Armstrong, R. He, and J.B. Zambon, J.B., 2010: Development of a Coupled Ocean-Atmosphere-Wave-Sediment Transport (COAWST) modeling system. Ocean Modeling, 35(3), 230-244, https://doi.org/10.1016/j.ocemod.2010.07.010.

The WAVEWATCH III® Development Group. 2019. “User Manual and System Documentation of WAVEWATCH III® Version 6.07.” Technical Note 333. College Park, MD, USA: NOAA/NWS/NCEP/MMAB.

Winant, C. D., Dorman, C. E., Friehe, C. A., & Beardsley, R. C. (1988). The marine layer off northern California: An example of supercritical channel flow. Journal of the Atmospheric Sciences, 45(23), 3588–3605. https://doi.org/10.1175/1520-0469(1988)045<3588:TMLONC>2.0.CO;2

Wu, W.-C., T. Wang, Z. Yang, and G. García-Medina, 2020: Development and validation of a high-resolution regional wave hindcast model for U.S. West Coast wave resource characterization. Renewable Energy, 152, 736–753. https://doi.org/10.1016/j.renene.2020.01.077.

Pacific Northwest National Laboratory

902 Battelle Boulevard
P.O. Box 999
Richland, WA 99354

1-888-375-PNNL (7665)

www.pnnl.gov